# Concurrent Geometrico-Topological Tuning of Nanoengineered Auxetic Lattices Fabricated by Material Extrusion for Enhancing Multifunctionality: Multiscale Experiments, Finite Element Modeling and Data-Driven Prediction

- J. Schneider <sup>a</sup>, M. Ebert <sup>b</sup>, R. Tipireddy <sup>c</sup>, V. R. Krishnamurthy <sup>b,e</sup>, E. Akleman <sup>d,e</sup>, S. Kumar <sup>a,f,\*</sup>
  - <sup>a</sup> James Watt School of Engineering, University of Glasgow, Glasgow, UK
- <sup>b</sup> J. Mike Walter '66 Department of Mechanical Engineering, Texas A&M University, College Station, USA
  - <sup>c</sup> General Motors, Palo Alto, California, USA
  - <sup>d</sup> Department of Visualization, Texas A&M University, College Station, USA
- <sup>e</sup> Department of Computer Science and Engineering, Texas A&M University, College Station, USA
  - f Glasgow Computational Engineering Centre, University of Glasgow, Glasgow, UK
    - \* Corresponding author. E-mail address: <a href="msv.kumar@glasgow.ac.uk">msv.kumar@glasgow.ac.uk</a> (S. Kumar)

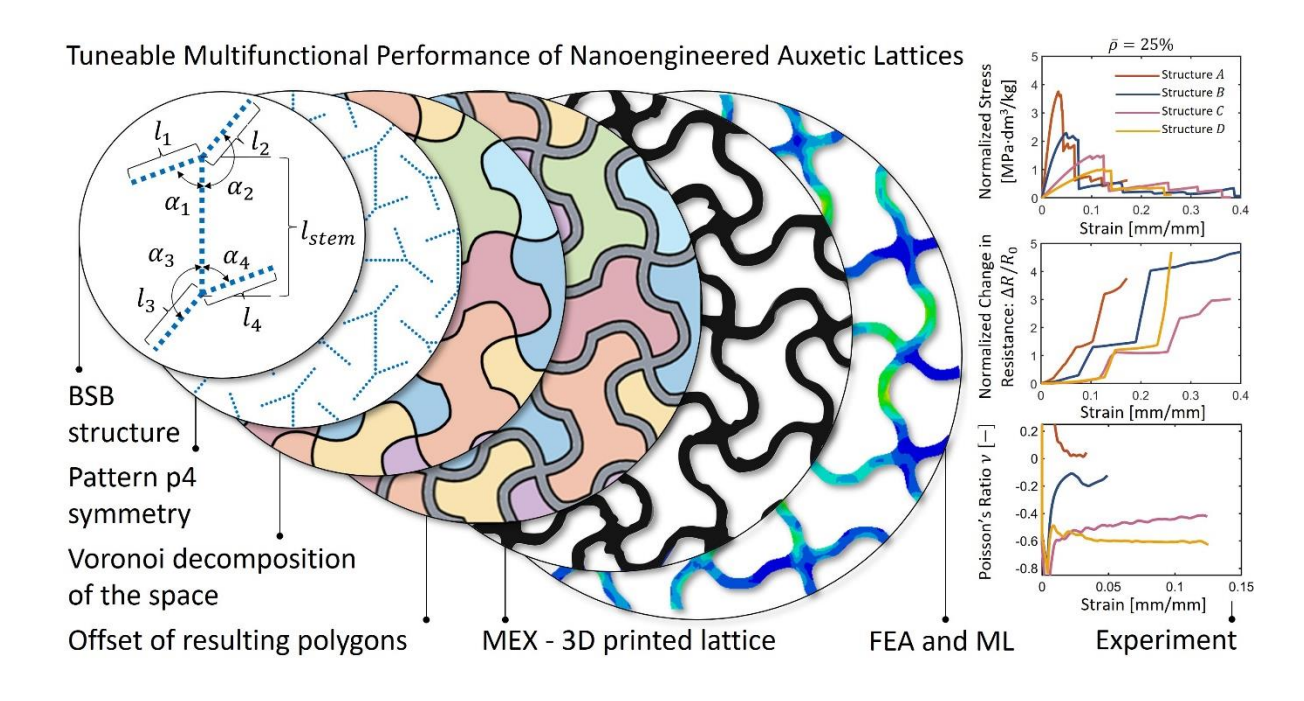
#### **Abstract**

This study demonstrates the multifunctional performance of innovative 2D auxetic lattices through a combination of multiscale experiments, finite element modeling and data-driven prediction. A geometric modeling approach utilizing Voronoi partitioning and a unique branchstem-branch (BSB) structure, patterned according to 2D wallpaper symmetries, enables precise concurrent geometric and topological tuning of lattices across a continuous parameter space. Selected architectures are physically realized via material extrusion of polylactic acid (PLA) infused with carbon black (CB). Experimental characterizations, supported by Finite Element modeling, reveal the significant influence of BSB structure's design parameters on mechanical and piezoresistive performance under tensile loading, with a remarkable Poisson's ratio of -0.74, accompanied by a 15-fold increase in elastic stiffness and a 34-fold increase in strain sensitivity. Additionally, architecturally, and topologically tailored lattice structures exhibit tunable damage sensitivity, reflecting the rate of conductive network destruction within the lattice. This offers insights into the rapidity of cell wall failure, with a steeper slope of the piezoresistance curve in the inelastic regime indicating a faster breakdown and quicker onset of mechanical failure. Integration of Gaussian Process Regression enables accurate exploration of the design space beyond realized structures, highlighting the potential of these intelligent lattice structures for applications such as sensors and in situ health monitoring, marking a significant advancement in multifunctional materials.

#### Keywords

Additive Manufacturing; Cellular Composites; Functional Materials; Auxetic Lattice Structures; Metamaterials

#### **Graphical Abstract**



# 1 Introduction

Additive Manufacturing (AM), commonly referred to as 3D printing, has experienced substantial growth in recent years due to its distinct advantages and the design freedom it offers in comparison to conventional manufacturing methods like injection molding or extrusion [1]. In the realm of AM, three-dimensional objects are produced in a layer-by-layer manner, guided by computer-aided design (CAD) models, with material extrusion (MEX) emerging as the predominant technique. This evolution in AM has substantially expanded the scope for creating intricately designed cellular architectures, surpassing the limitations of traditional manufacturing. This trend has been particularly driven by industries such as aerospace, automotive and sports, leading to an augmented demand for innovative lightweight materials characterized by outstanding mass specific mechanical properties such as specific stiffness, strength, and energy absorption capabilities. The integration of engineered cellular structures has been instrumental in minimizing material consumption by selectively applying it where essential [2]. These cellular structures are categorized into periodic porous configurations or random stochastic foam structures, the former being comprised of standardized and modifiable repeating unit cells, while all have found significant utility in energy-absorbing applications, owing to their organized or randomized porous architecture [3].

Periodic and aperiodic cellular materials differ fundamentally in their structural configurations, impacting their mechanical and physical properties. Lattice structures, characterized by their periodic arrangement of unit cells (e.g. Gyroid, Octet, Kelvin, Simple Cubic), offer high precision and repeatability in their mechanical response [4,5]. This regularity facilitates the customization of mechanical properties, such as stiffness and strength, through the modification of unit cell geometry. On the other hand, aperiodic materials (e.g. Spinodoid, Voronoi-based, stochastic foams), exhibit a more irregular and less predictable pattern. All these cellular materials usually exhibit a strong coupling between macroscopic properties and relative density (solid volume fraction,  $\bar{\rho} = \rho_c/\rho_s$ , with  $\rho_c$  and  $\rho_s$  representing the densities of cellular and solid material respectively) of the cellular structure because the solid material is weakened by the engineered porous architecture. However, the degree of such coupling can be tuned by controlling the porous architecture and perhaps, can be fully decoupled by creating micro- and nano-architected porous architectures, usually referred to as metamaterials.

Contrary to what one might expect, deviating from the periodic structure typical of classical metamaterials can be key to accessing a vast range of properties and facilitating the seamless integration of function grading [6]. In their review, Zaiser and Zapperi [7] highlight that while

mechanical metamaterials are traditionally periodic, introducing disorder into their design has shown to enhance their mechanical performance, drawing parallels with the advantageous properties of biological materials with disordered structures. They explore both the opportunities and challenges presented by randomness in these materials, underscoring emerging algorithmic and data-driven approaches for optimizing disordered mechanical metamaterials. Expanding the design spectrum to include random, disordered structures alongside periodic ones opens avenues for unforeseen solutions, which can offer not only enhanced mechanical efficiency but also greater resilience and fault tolerance compared to their ordered counterparts [7].

Furthermore, explorations extend towards investigating distinctive properties, such as negative Poisson's ratios, negative stiffness and negative compressibility [8]. Metamaterials showcase unprecedented traits rarely encountered in natural materials [9–11]. Their overall performance at the macroscopic level is intricately defined by their micro- or nano-scale architecture, often achievable through AM. By replicating isotropic or orthotropic unit cells at small length scales across two or three dimensions, the desired macroscale material attributes can be realized. Moreover, the incorporation of electrically conductive fillers, primarily carbon-based, including carbon fibers (CF), carbon nanotubes (CNT), graphene nano-platelets (GNP), or carbon black (CB), into polymeric matrices bestows them with electrical conductivity, enabling the attainment of piezoresistive attributes [12,13]. These materials, recognized as smart materials, are endowed with self-sensing capabilities.

Studies such as those by Chen et al. [14], underline the significant advancements and potential of AM in producing complex-shaped electronic devices, focusing on piezoelectric materials. Their review summarizes the current status, challenges, and future research directions in this field, emphasizing the development of high-performance piezoelectric devices with wide-ranging applications. Verma et al. [12] introduce a method for 3D printing self-sensing, piezoresistive materials using polypropylene reinforced with CNTs, enhancing their mechanical and electrical properties, and demonstrating their potential in biomedical applications like orthopedic braces. Ubaid et al. [15] present an investigation into AM of self-sensing cellular composites using CNT-filled polypropylene filaments, demonstrating their tunable sensing capabilities and improved mechanical performance, with potential applications in custom biomedical devices. Sanz-Pena et al. [16] focus on developing wearable piezoresistive sensors for gait rehabilitation, using AM to create mechanical metamaterials with pressure-sensing capabilities. It explores different structural designs and graphene infusion processes to customize the sensors' measuring range and sensitivity, highlighting the potential of designing wearable sensors with predictable responses based on

their structure and materials. Schneider et al. [17] explore the mechanical, self-sensing, and biological properties of 3D-printed PEEK composite scaffolds reinforced with CNTs and GNPs, demonstrating high strength, durability and cytocompatibility, offering the potential for advanced bone tissue engineering implants with intelligent features.

In contrast to conventional materials that typically contract transversely when stretched longitudinally and expand when compressed, auxetic materials demonstrate a counterintuitive behavior [18]. They contract laterally when compressed and expand when stretched longitudinally (Figure S1, Supporting Information (SI)). This behavior is quantified by the negative Poisson's ratio ( $\nu$ ), which is a negative ratio of transverse to axial strain, i. e.,  $-\varepsilon_{trans}/\varepsilon_{axial}$  with  $\varepsilon$  being the axial and transverse strain. While standard materials exhibit a positive Poisson's ratio, auxetic materials display a negative ratio, ranging from values just below 0 down to -1 for isotropic materials. Although auxetic structures are uncommon in nature, they have been observed in minerals and other contexts [19,20].

The intrigue surrounding auxetic materials is not solely centered on their unconventional mechanical responses; it extends to their capacity to achieve other remarkable mechanical attributes. The negative Poisson's ratio prompts significant alterations in Young's modulus (E) and shear modulus (G). The resultant twisting or tearing forces within these structures confer increased resistance to shear, given by  $G = E/(2(1+\nu))$ , where G and E are shear and Young's moduli respectively. Notably, whereas traditional materials often exhibit Young's modulus that is at least twice that of the shear modulus, auxetic materials can achieve a balance at  $\nu = -0.5$  [21], where the Young's modulus equals the shear modulus.

Extensive research has been devoted to two-dimensional auxetic structures [22–28], yielding three main types categorized by their deformation patterns. This includes the honeycomb-based reentrant structure, which stands apart from regular honeycomb unit cells due to its anisotropic nature, resulting in enhanced transverse Young's and shear moduli [29]. Another prevalent category involves chiral or anti-chiral units, where auxeticity emerges from the configuration of straight ligaments linked at central circular nodes, facilitating auxetic behavior through rotational motion [30]. Unlike reentrant cells, chiral structures maintain a constant negative Poisson's ratio over a wider range of strain, up to 25% [31]. A third mechanism employs hinged rotation squares, as proposed by Grima et al. [32]. All these configurations extend to a three-dimensional realm, with the foundational 2D structure preserved. Yang et al. [29] demonstrated this with 3D reentrant structures, and Ha et al. [31] applied it to chiral structures. Recent studies expand to applications such as auxetic foams, utilized for acoustic wave and shock energy dissipation [33,34], and auxetic yarns for advanced textiles [35]. Other recent advancements include a novel prefabricated auxetic honeycomb meta-structure based

on mortise and tenon principles offering cost-effective fabrication options [28], an innovative re-entrant auxetic honeycomb with zigzag inclined ligaments enhancing stiffness without compromising auxeticity [36], and a novel 3D tetra-missing rib auxetic structure featuring tension/compression-twisting effects for tunable mechanical properties [37]. These developments highlight the ongoing innovation in the field, demonstrating the adaptability and potential for a variety of applications.

Auxetic materials find broad applicability, particularly in scenarios demanding substantial shear resistance, improved hardness, reduced fatigue crack propagation, superior toughness and modulus resilience, or effective vibration absorption. In the medical domain, auxetic materials hold potential for applications like smart bandages that release wound-healing agents based on wound swelling [38], and self-healing membranes or films that mend tears due to their inherent closing mechanism [39]. Additionally, 2D auxetic structures can serve as flexible electronic devices, altering resistance with physical deformation to offer insight into the material shape, as demonstrated by Ren et al. [40], making them suitable for wearable electronics.

This study centers on the creation of innovative two-dimensional auxetic structures with tunable piezoresistive self-sensing capabilities. This innovation stems from a recent geometric modeling paradigm for designing space-filling shapes based on Voronoi partitioning of space generated by symmetric arrangements of high-dimensional Voronoi sites. Traditionally, Voronoi partitions are computed by using points as sites resulting in convex polygonal (in 2D) or polyhedral (in 3D) partitions with planar boundaries. When these sites are arranged according to some spatial symmetry, the resulting Voronoi cells are guaranteed to be congruent (i.e. the entire tessellation can be composed by repeating a single unit cell). The unit cell is therefore space-filling, i.e. a single shape can tile the entire space [41]. In recent years, this idea has led to several classes of 3D lattices by utilizing higher-dimensional Voronoi sites such as lines, curves and even surfaces in 3D space [42-44]. The use of higher dimensional sites leads to a vast design space of space-filling shapes that are not restricted to be convex or planar anymore. What is further interesting is that each type of spatial symmetry and class of Voronoi sites leads to a completely different design space for generating different types of architected materials such as topologically interlocked materials [42,44] or geometrically interlocked materials [43]. Recently, it was shown that a combination of lines as Voronoi sites arranged using 2D weave patterns may also lead to a class of 2D auxetic lattices [45]. However, a fundamental limitation of this approach is that it lacks an intuitive mapping between the geometry of the unit cells to the resulting behavior due to a discrete parameter space constrained by weave patterns. Our key insight in this work is that the choice of spatial symmetry and the design of the Voronoi site are both essential to enable systematic control, tuning and prediction of the mechanical behaviors of such lattices. Specifically, the symmetry must enforce auxeticity while the geometry of the Voronoi site must allow for a continuous parameter space. Using this as our rationale, we develop a novel approach for generating a new class of space-filling shapes that lead to a systematically tunable design space of auxetic lattices. Our approach focuses on a specific type of symmetry, namely the p4 wallpaper group, and a novel Voronoi site geometry based on connected acyclic graphs (trees) that serve as medial representations for the lattice design space. Specifically, we leverage a unique branch-stem-branch (BSB) structure as the design template for the Voronoi site. Unlike the existing research on implicit generation of 2D auxetic lattices, this choice of Voronoi site is grounded in the theory of medial geometries. In totality, the choice of p4 symmetry ensures that the lattices are auxetic and the choice of BSB sites offers a continuous parametric space based on stem/branch lengths and branch angles thereby enabling both tuning and optimization of the Poisson's ratio of the resulting lattices.

A selected set of lattices is produced through MEX using CB-infused PLA filament feedstock. The intricate interplay among key design parameters - specifically, stem length, branch angle and branch length - and the resulting mechanical and piezoresistive properties of the fabricated PLA/CB nanocomposite auxetics under tensile loading is thoroughly examined. The focus is on concurrent geometrico-topological tuning, achieved through the geometric modeling approach integrating Voronoi partition of the Euclidean plane space using BSB sites arranged according to p4 wallpaper symmetries. The significance of concurrent geometricotopological tuning is evident in the exceptional mechanical properties and piezoresistive selfsensing performance observed in the selected auxetic structures of the same mass and parent composite. By combining finite element modeling and machine learning tools, the predictions not only validate experimental findings but also extend exploration into a vast design space beyond the structures realized experimentally. Strategic manipulation of design parameters within the BSB structure, and consequently, the unit cell architecture, is demonstrated to significantly improve both the mechanical performance and piezoresistive behavior of the structures. This has the potential to enhance elastic stiffness, auxeticity, gauge factor (a measure of strain sensitivity in the elastic regime), and damage sensitivity (a measure of the rate of destruction of the conductive network in the structure under tension in the inelastic regime). The study highlights the potential of lattice structures, particularly in applications where in situ health monitoring and auxetic deformation are crucial.

## 2 Materials and Methods

#### 2.1 Geometric modeling of 2D lattices

To conceptualize the tunable lattice modeling approach, our fundamental need is to develop concurrent parametrization for both the geometry and the topology of the auxetic lattices. For this, we begin with the observation that we can view 2D auxetic lattices as 2-honeycombs which are generalizations of the hexagonal honeycombs. In geometry, a honeycomb is simply a tessellation of space. For 2D auxetic structures with a single repeating unit cell geometry, these 2-honeycombs are further cell-transitive, meaning that they can be defined based on some 2D spatial symmetry groups (also known as wallpaper groups). From this perspective, the ligaments of the auxetic lattice (or for that matter, any lattice) is simply a thickened version of the boundaries of the cells of the honeycomb. In this context, we note that auxetic behavior that is observed in currently known geometries shares a common geometric principle that is linked to the nature of symmetry in the entire lattice. Here, we invoke the fact that arranging Voronoi sites according to a given symmetry group leads to a cell-transitive honeycomb after Voronoi partition (also known as Dirichlet Domains) [41]. Under this principle of geometric construction, we point out p4, p4m, p6, and p6m symmetry groups are most prevalently used to generate auxetic behaviors [29-32]. Having said this, mere symmetry is not sufficient for producing auxetic behavior. That behavior is induced by the specific geometry (i.e. reentrant, chiral, rotational) at the junction points of the ligaments of neighboring unit cells [29–32]. The aim of this paper is to resolve both these components, namely lattice symmetry and the shape at the junction point, through a single integrated approach to concurrently control both the geometry and topology of the lattices.

#### 2.1.1 Conceptual framework for geometrico-topological tuning

The design space corresponding to the symmetry groups is discrete and each symmetry group is likely to provide a completely distinct design space of lattices making systematic design intractable and untunable [45]. Therefore, we first fix the symmetry group to p4 to scope our investigation. The p4 symmetry group offers a geometrically and topologically stable parametrization specifically in the context of Voronoi partitioning. As such our method will identically apply to any chosen symmetry group and is therefore general. What is important to note here is that the cell-transitivity resulting from wallpaper groups can be a useful geometric property to ensure periodic transmission of load through the lattice thus making is more predictable and controllable unlike other works that either develop random auxetic lattices [46] or lattices based on other types of symmetries such as weaves [45].

The second critical aspect of our approach stems from the shared geometric characteristic observed in all, the reentrant, chiral, and rotational mechanisms. This is where the choice of a well-designed Voronoi site geometry is essential to enable concurrent geometric and topological tuning in a systematic and continuous parameter space. Ideally, the site should allow for complete control of the junction geometry while maintaining the lattice topology (which was induced by the p4 symmetry group). To achieve this objective, we refer to our choice of p4 symmetry and note that the canonical tessellation corresponding to p4 is simply a rectangular tessellation of space. As such, one may simply choose the simplest site geometry of a higher dimension than a point, i.e. a line segment [45]. However, the ability for local geometric control at the ligament junctions is impossible with a line segment simply because the only parameter available for such control is its length and orientation. On the other hand, note that an individual unit rectangular cell in a p4 tessellation is uniquely described by the branch-stem-branch structure which is the medial axis of this rectangle (Figure 1a). This medial axis, therefore, provides a natural choice for Voronoi sites. Here, the extremities of each branch control the local geometry of its closest junction while the stem maintains the overarching shape of the cell leading to a highly tunable continuous design space. Below, these insights are used to detail the procedure to generate 2D auxetic lattices.

#### 2.1.2 Algorithmic procedure for lattice generation

To put the presented concepts into practice, the first step of the lattice generation process is to create an arrangement of the BSB structure in the Euclidean plane based on p4 symmetry. Recall that this structure is the medial axis of a unit tile in a regular rectangular tessellation. Without loss of generality, a square grid is assumed with each square. Therefore, a unit BSB structure is initialized within a rectangular domain. The structure is composed of a vertical line acting as the stem and a total of four branches (two branches at each extremity of the stem), as depicted in Figure 1b. The stem and its corresponding branches are patterned in the plane based on the p4 wallpaper symmetry. To do so, the procedure is to first create a group of four cells, each containing one BSB site such that each cell is orthogonal (at an angle of 90°) to its neighboring cell. Repeating this group of four cells in the plane directly gives the arrangement of sites (depicted in Figure 1c). The next step is to compute the Voronoi partitioning of this arrangement of sites. For this, we employ the strategy used by prior works [42]. Specifically, equidistant points are sampled on each of the BSB sites and Voronoi partitioning is computed for those points. A subsequent Boolean of all Voronoi partitions belonging to points from the same BSB site results in the final tessellation of the plane with respect to the BSB sites (depicted in Figure 1d). Note that this combination of arrangements based on wallpaper symmetry with Voronoi tessellation naturally leads to the generation of a space-filling shape (i.e. a single unit shape that can tile the entire plane) as the unit cell. Following Voronoi partitioning, the boundaries of each cell in the resulting tessellation (cell-transitive 2-honeycomb) is thickened by generating an inward offset and subsequent subtraction from the initial tessellation. This results in the formation of the in-plane structure of the lattice (as depicted in Figure 1g). To enable numerical and experimental samples, two end pieces are further added to the structure. Finally, this 2D thickened structure is extruded to produce a lattice structure suitable for printing and simulation purposes (Figure 1h). Moreover, supplementary video 1 (SV1) illustrates an animated version of this geometry generation process, providing a dynamic visualization of the stages from initial line arrangement to the final extruded lattice.

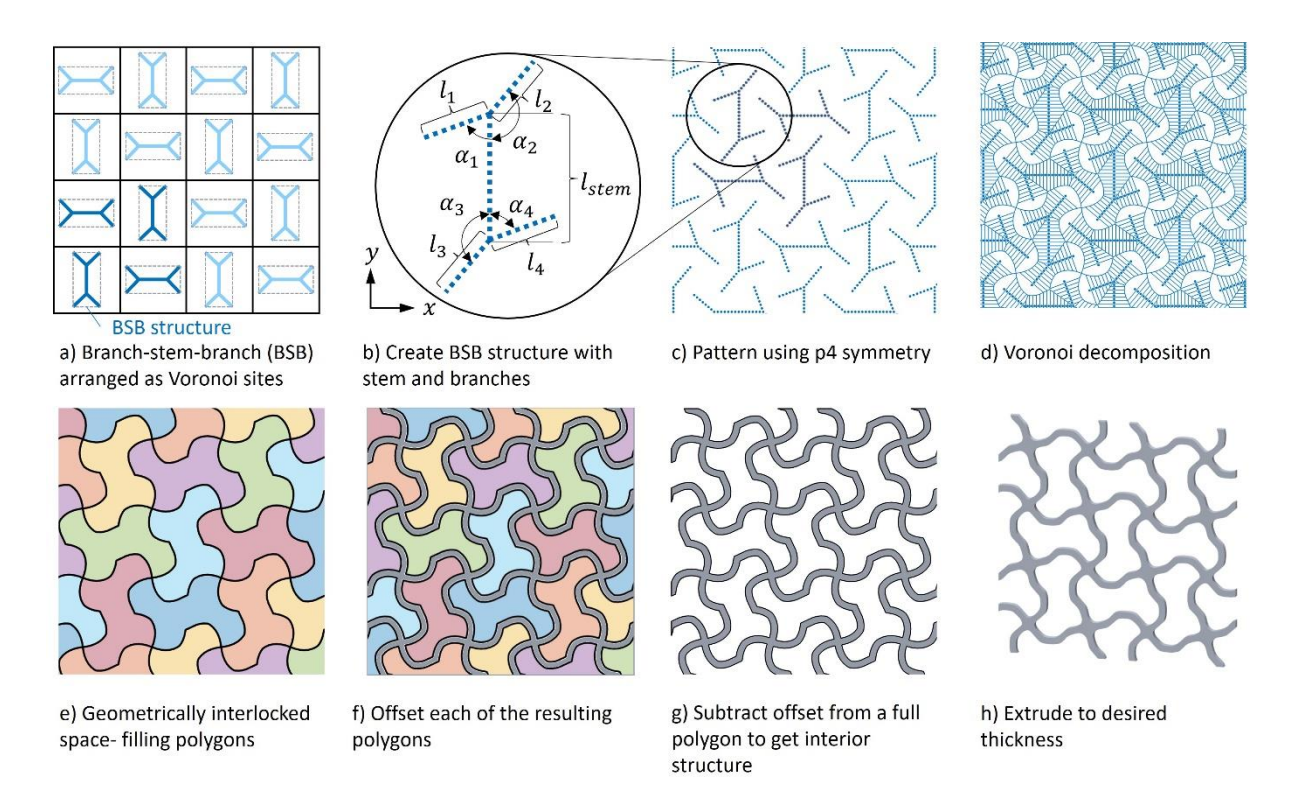


Figure 1. The computational pipeline employed to create a wide range of auxetic shapes using a parameterized design space: It begins with the conceptualization of the branch-stem-branch (BSB) structure, as shown in tile a). This structure is based on the medial axis of the rectangular cell, corresponding to the p4 symmetry group and represents the fundamental pattern from which the subsequent designs are derived. The BSB structures are arranged as Voronoi sites within the Euclidean plane, based on p4 symmetry, setting the groundwork for the iterative design process. From tile b) onwards, the development of the BSB structure commences with stem and branches, evolving through pattern creation using p4 symmetry (c), Voronoi decomposition (d), and the formation of geometrically interlocked space-filling polygons (e). The ensuing steps involve offsetting each polygon (f), subtracting the offset to reveal the interior structure (g), and finally, extruding these shapes to the desired thickness to realize the auxetic forms (h).

#### 2.1.3 Parameterization of auxetic lattice structures

The topology of the cellular geometry can be controlled by various parameters, thereby enabling the creation of a diverse range of lattices.

#### 2.1.3.1 Variation in stem dimensions

There are two ways to manipulate and alter the stem. One is by adjusting the angle of the stem in relation to its p4 pattern symmetry angle, and the other is by modifying the length of the line. Altering the angle significantly impacts the resulting polygon. For instance, in scenarios where no branches are attached to the line ends, varying the angle gradually transforms the polygon. This transformation continues until reaching a 45° rotation, where the polygon becomes a square. For angles exceeding 45°, the outcome mirrors an angle less than 45°. Adjusting the line length affects the shape of the parabola formed from the interaction between the end of a line segment and the line segment of an adjacent shape. This becomes evident as the line length approaches zero, resulting in a singular point representing that specific stem and a resulting square grid. Conversely, elongating the line produces a parabola with a steep slope in the Voronoi decomposition, as depicted in Figure 2a,d. An important point to note is that the cases shown in 2a-d are essentially the same as the weave-based auxetics recently introduced in the literature [43]. The specific weave parameters here are based on the trivial plain weave. These cases specifically demonstrate the limitation of using weave symmetries in enabling local tunability at the junction points. By reformulating lattice generation as a combination of wallpaper groups and medial geometry, the approach in this paper departs significantly from current works by allowing for complete control of junction geometry, which is fundamentally responsible for auxetic behavior.

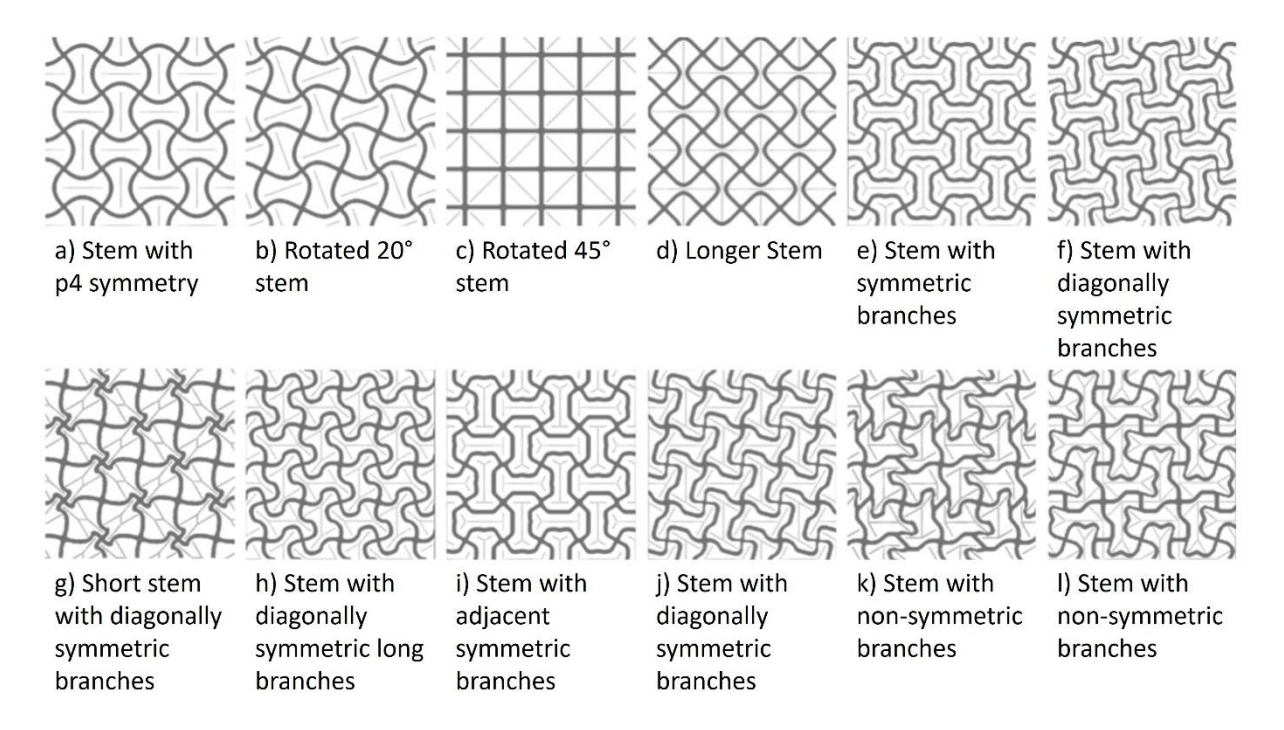


Figure 2. Different parameters shape output with the corresponding complex medial axis overlaid. Each shape has a description of the changes made to the stem or the branches. Note that cases a-d) are examples with no branching. In these cases, no local tuning is possible at the junction points. Further, notice that the topology of the tessellations is not

necessarily uniform. For instance, case k) contains vertices with valency 3 and vertices with valency 4.

#### 2.1.3.2 Alterations in branch geometry

Each branch emanates from the stem's end, featuring designated length and angle values that dictate its trajectory relative to the stem. For every individual branch, specific length and angle values are provided as inputs, alongside the option to incorporate a desired type of symmetry.

The branches can exhibit complete asymmetry from one another (as depicted in Figure 2k,i), diagonal symmetry (as seen in Figure 2f,g,h,j), adjacency symmetry (as presented in Figure 2l), or full symmetry (illustrated in Figure 2e). While full independence between all branches entails a total of 8 parameters that need to be configured, greater levels of symmetry result in a reduced number of required parameters.

#### 2.1.3.3 Modifications in structural thickness

The shape's thickness is determined by the offset process (depicted in Figure 1f). This offset parameter regulates the overall relative density (solid volume fraction) of the resulting cellular structure. A zero offset would render the shape entirely hollow, while a significantly large offset would yield a shape with complete surface coverage. Moreover, extremely large offsets lead to a loss of the shape's defining characteristics, owing to the substantial contraction of the overall Voronoi region.

#### 2.1.3.4 Tailoring relative density

The relative density of the cellular structures,  $\bar{\rho}$ , is ascertained through a comparison of its volume to that of a fully solid block occupying equivalent space. Here, density values were adjusted to predetermined ranges between 10% and 30% in 5% increments. Modifying the ligament thickness for a given topology served as the mechanism for altering relative density. Increasing the thickness equates to a greater volume, consequently raising the relative density. When necessitated to attain a specific density, adjusting the shape's thickness can be undertaken until the desired density value is achieved.

#### 2.1.3.5 Implementation of shape generation and selection

The process of shape creation was automated using Houdini Apprentice 18.5.563, enabling the seamless execution of the described procedure. Through this tool, a diverse array of lattices could be generated. Herein, the process was employed to generate both familiar auxetic structures and previously unknown auxetic structures. This approach aimed to assess the distinct characteristics of these geometries. Three sets, each consisting of four designs

(as listed in Table S1), were produced. This yields a total of 60 options when considering the various relative densities, of which 56 were manufactured.

# 2.2 Material extrusion additive manufacturing of bulk and nanoengineered lattice structures

2D Auxetic lattice structures were manufactured using the MEX 3D printing technique. In MEX, the feedstock is melted and deposited onto a heated platform through a heated nozzle in a layer-by-layer manner, following the predetermined path in CAD design. The feedstock comes in filament form with a diameter of 1.75 mm. For this study, PLA with carbon black filler (PLA/CB) from Proto-pasta (ProtoPlant, makers of Proto-pasta, USA) was utilized. This material comprises Natureworks 4043D PLA, a dispersant and conductive carbon black.

A Flashforge Creator Pro (Zhejiang Flashforge 3D Technology Co., LTD, China) 3D printer was employed for fabricating the 2D lattice structures, utilizing a nozzle with a 0.4 mm extrusion diameter. The molded resin's volume resistivity is reported as 15  $\Omega$ ·cm, while for 3D printed parts along the layers (x-y plane), it is 30  $\Omega$ ·cm and against the layers (z, out-of-plane), it is 115  $\Omega$ ·cm [47]. The resistance of a 10 cm length filament with a 1.75 mm diameter measures 2-3 k $\Omega$  [47]. The density is 1.24 g/cm³ and the melting point onset is 155 °C [47].

The printing parameters were iteratively defined and adjusted to achieve consistent print quality, reduced porosity, high dimensional accuracy, and superior surface quality. The primary layer height was set to 0.18 mm, infill density at 100%, bed temperature at 60 °C, and nozzle temperature at 220 °C. Introducing an extrusion multiplier of 1.05 improved print quality by reducing porosity. The extrusion width was 0.48 mm, while for structures with smaller feature sizes ( $t < 0.48 \, mm$ ), the extrusion width was decreased to achieve the designed sizes. Each geometry is printed and tested at least three times to ensure repeatability. All lattices were printed in a size of  $50 \ mm \times 50 \ mm \times 1 \ mm$ . Adjacent to the cellular structure, a solid part with a constant thickness was printed to grip the specimen to the machine during testing. Realizing lattices with a range of topologies at similar relative densities enabled the comparison of mechanical and electrical performance for similar densities, facilitating the evaluation of the best-performing structure under defined parameters for a given weight. In addition to lattice structures, bulk specimens for tensile, compression and three-point bending tests were printed in accordance with ASTM D638, ASTM D695, and ASTM D790, respectively. Notably, the printing outcomes were deemed satisfactory, faithfully replicating the CAD model. However, upon microscopic examination, slight over-extrusion of ligaments was observed.

#### 2.3 Protocols for mechanical characterization and testing

Tensile tests on lattice structures and bulk (fully dense) materials were conducted using a Zwick Roell Z2.0 universal testing machine (UTM) equipped with a 2.5 kN load cell. Compression and three-point bending tests on bulk specimens were carried out on a Zwick Roell Z250 UTM with a 250 kN load cell. Cellular samples under tension and bulk specimen under compression were tested at a speed of 5 mm/min, whereas for bulk specimens under tension and bending the speed was reduced to 2 mm/min. For tension and compression tests, the engineering stress ( $\sigma$ ) was determined using the measured load (F) from the UTM's load cell and the cross-sectional area (A) of the specimen, following the equation  $\sigma = F/A$ . Engineering strain was recorded as a function of  $\Delta l$  as  $\varepsilon = \Delta l/l_0$ , where  $\Delta l$  is the change in length of the sample in the loading direction, and  $l_0$  is the initial sample length.

In three-point bending, the flexural stress  $(\sigma_f)$  is calculated as  $\sigma_f = 3PL/2bd^2$  and the flexural strain  $(\varepsilon_f)$  as  $\varepsilon_f = 6Dd/L^2$  where P is the load at any instant, L is the support span, d is the specimen depth, and D is the midspan deflection. The flexural modulus  $(E_b)$  can be calculated as  $E_b = L^3m/4bd^3$  with m representing the slope of the tangent to the initial straight-line portion of the load-deflection curve [48].

For lattice structures the strain was calculated using the displacement obtained from the UTM, while for bulk tensile specimens, the strain was captured via digital image correlation (DIC). In DIC, the strain is calculated by monitoring the deformation optically using a digital camera, while specimens were prepared by adding a high-resolution speckle pattern via spray paint on the observed surfaces. The Vic-2D 2009 (Correlated Solutions, Inc., USA) software was used to calculate the strain. The initial linear slope of the stress-strain response allows for the calculation of stiffness in terms of Young's modulus (E), with  $E = \sigma/\varepsilon$ . The maximum strength is determined as the peak stress measured during testing. The energy absorbed is obtained by integrating the stress-strain response up to failure, given by

$$W = \int_0^{\varepsilon_d} \sigma(\varepsilon) d\varepsilon \tag{1}$$

where  $\varepsilon_d$  represents the densification strain or strain at breakage for compression and tension tests, respectively. For cellular structures, specific energy absorbed is normalized by density and reported as

$$W = 1/\rho_c \int_0^{\varepsilon_p} \sigma(\varepsilon) d\varepsilon \tag{2}$$

in J/kg, where  $\rho_c$  is the density of the cellular structure and  $\varepsilon_p$  is the strain at first ligament breakage. The specific energy absorption efficiency,  $\eta$  is calculated as

$$\eta = 1/(\sigma_p \, \varepsilon_p) \int_0^{\varepsilon_p} \sigma(\varepsilon) d\varepsilon \tag{3}$$

where the index p specifies the instant of first ligament breakage.

In addition to evaluating mechanical performance as described above, the electrical resistance of the structures at any instant of loading (R) and the fractional change in resistance as a function of strain,  $\Delta R/R_0$ , were measured and calculated, respectively, where  $R_0$  is the resistance of the sample with no load applied. This enables the calculation of the gauge factor (in the elastic regime) as

$$k = (\Delta R/R_0)/\varepsilon = (1+2\nu) + (\Delta \rho/\rho_0)/\varepsilon \tag{4}$$

with  $\varepsilon=(l_T-l_0)/l_0$ , and  $l_0$  representing the initial (unstrained) length of the tested structure. Note that  $\Delta\rho/\rho_0$  indicates relative change in resistivity and this contribution becomes predominant in nano reinforced composites.

The resistance was measured *in situ* using a Fluke 8846A digital bench multimeter, capable of measuring a range from 10  $\Omega$  to 1  $G\Omega$  with up to 10  $\mu\Omega$  resolution. To facilitate this measurement, the samples were insulated from the machine grips, and conductive copper layers were attached to them, enabling the measurement of resistance as a function of strain excluding the machine's resistance (Figure 3).

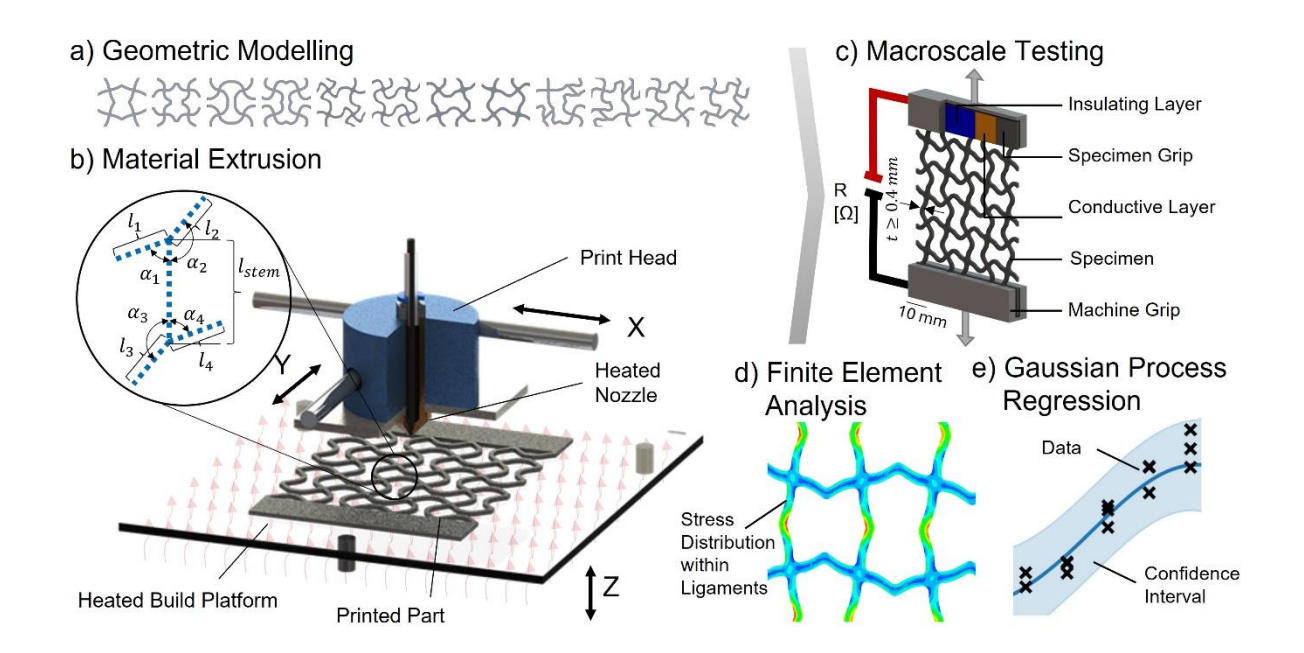


Figure 3. a) Schematic representation of the a) exemplary geometries (unit cells) developed in this study, b) illustration of the Material Extrusion (MEX) AM process, c) mechanical & piezoresistive macroscale testing, d) finite element analysis setup depicting stress distribution in the lattice structure, and e) gaussian process regression used to extrapolate the design space from experimental data.

The lateral displacement of the samples under applied tensile load was tracked using a digital camera focused on the central region of the specimens. The lateral strain was determined through analysis of image sequences using a developed script, supported by relevant literature such as Yolcu and Baba [49]. Initially, the image data was imported and transformed into a binary image, facilitating the subsequent labeling of individual and distinct sections of the lattice structure for analysis. In the subsequent stage, the primary portion of the undamaged lattice structure was identified and outlined, and the change in width was documented and synchronized with the axial displacement data from the testing machine (depicted in Figure S2). With axial and lateral displacements identified, the Poisson's ratio ( $\nu$ ) is calculated as  $\nu = -\varepsilon_{trans}/\varepsilon_{axial}$  and depicted graphically as a function of axial strain.

#### 2.4 Finite element modeling

Dynamic, explicit Finite Element Analysis (FEA) was performed on lattice structures using Abaqus 2020 (Dassault Systèmes) FE software to support experimental findings and establish a predictive capability of the cellular structures under tensile loading conditions. A Drucker-Prager (DP) material model was chosen to reflect the response of PLA/CB bulk material under tensile and compressive loading conditions. It employs a pressure-dependent yield criterion, which means that the material's strength is influenced by the hydrostatic stress acting on it. During small deformations leading up to the material's yield point, the model assumes linear

elasticity. Following material yielding, the plastic flow rule dictates the plastic deformation behavior, with plastic flow associated with an equivalent plastic strain determined by the deviatoric stress state. The DP model allows for isotropic hardening, meaning the material's strength increases as it undergoes plastic deformation, a phenomenon controlled by parameters such as the dilation angle. Detailed information on this model can be found in the Abaqus manual [50].

The linear elastic properties of the DP material model were identified using the tensile stressstrain response of the bulk PLA/CB composite, with a Young's modulus calculated as 1.5 GPa and a Poisson's ratio obtained as 0.46 through DIC. The DP hardening behavior was characterized by establishing a correlation between the yield stress and the absolute plastic strain derived from the tensile test data. To account for the mismatch between the compressive strength (64 MPa) and tensile strength (40 MPa) of the bulk material, both the angle of friction and the angle of dilation were set at 20°, with a flow stress ratio of 1. Notably, dilatancy effects were considered ineffective due to the assumption of ductile deformation being linked to shear yielding, leading to the equality of the angle of dilation with the angle of friction. In order to accurately assess the deformation characteristics of lattice structures, geometric nonlinearity was considered, alongside material nonlinear effects. To address failure, a ductile damage model was implemented, which considered a fracture strain of 0.12 and 1 at a stress triaxiality of 0.33 and -0.33, respectively. The damage evolution was assumed to follow a linear softening pattern and was considered to be independent of the strain rate. These settings were iteratively refined through tension and compression simulations of both bulk and lattice structures, which substantiated the modeling choices and replicated the materials' performance effectively. During bulk material calibration, a minor difference in the elastic moduli was observed between tension and compression. This difference in Young's moduli stems from a combination of microstructural features and material anisotropy associated with layer-by-layer additive manufacturing process. In tensile tests the beads are parallel to the direction of loading, while in compression tests beads are orthogonal to the loading direction. The resultant variation in inter- and intra-bead porosity and material anisotropy significantly impacts performance [51,52]. Acknowledging that tensile deformation is dominant in the lattice structures under examination, with ligaments aligned along the extrusion path, calibration prioritized the tensile response. Consequently, the compressive modulus in the FE model was conservatively overestimated. While this study exclusively examined mono-modulus elastic behavior associated with the DP model under tensile loading, it's worth noting that a material model featuring bi-modulus elastic behavior can be implemented in Abaqus using User Material Subroutines (UMAT).

To capture the mechanical response of the lattice structures accurately, the FE mesh was constructed using CPS4R elements. These four-node bilinear plane stress quadrilaterals were selected for their computational robustness, each with an average size of 0.33 mm, ensuring a minimum of three elements spanned the width of each ligament for detailed stress mapping. Mesh refinement was strategically increased at the joints to accurately capture stress concentrations. The elements were designated with reduced integration and a single integration point to enhance computational efficiency and reduce the potential for locking effects, which can skew results in bending-dominated scenarios. Hourglass control mechanisms were activated within the elements to counteract zero-energy deformation modes that can arise from reduced integration schemes. Convergence analysis was conducted to confirm the appropriateness of the mesh size, ensuring that numerical accuracy was not compromised in the pursuit of computational efficiency. For regions undergoing failure, element deletion was enabled, allowing for the simulation to represent material separation and damage realistically. In alignment with the experimental protocol, the FE model's boundary conditions were appropriately defined. The bottom nodes were fixed in all directions, providing an encastre condition that mimics the physical constraints of the testing apparatus. In contrast, the top nodes were restricted to move only in the loading direction, mirroring the experimental loading speed. This setup was sustained throughout the simulation up to the point of ligament failure. Such detailed FE modeling ensures that the simulation closely parallels the experimental environment, thus accurately reflecting the response of the PLA/CB composite lattices under applied loads.

#### 2.5 Gaussian process regression for predictive modeling

In transitioning from mechanical testing to reliable predictive modeling, this section introduces Gaussian Process Regression (GPR) as a sophisticated machine-learning technique to extrapolate and understand the mechanical and piezoresistive behaviors of 2D auxetic structures from the gathered data [53]. Tensile test data from 2D auxetic lattice structures were imported into a Python environment and structured as a DataFrame using the pandas library, forming the foundation for subsequent analyses. Outliers were removed to enhance dataset quality. Specimen identifiers were used to extract relative density and integrate it into the data structure. This refined data was then segmented into unique subsets based on specimen names, facilitating individualized analyses.

Consider a data set  $D = \{x_i, y_i = f(x_i)\}, i = 1, \dots, n \text{ consisting of } n \text{ observations of input } x \text{ and output } y.$  We approximate the unknown function f as a Gaussian Process (GP) model of the form:

$$f \sim GP(m(x), k(x, x'; \theta)) \tag{5}$$

Where m is the mean function, k is the covariance kernel and  $\theta \sim p(\theta)$  are hyper parameters of the Gaussian process model. We employ squared exponential Kernel as the covariance function given by

$$k(x, x') = \sigma^2 e^{\frac{(x-x')^2}{2l^2}}$$
 (6)

where  $\sigma$  is the standard deviation and l is the correlation length which are hyper parameters that are estimated from the training data.

Here, we model mechanical/piezoresistive properties y as output and relative density as the input variable x for the GP model for each of the topologies. We estimate the parameters  $\theta$  of the Gaussian process by maximizing the log marginal likelihood given by

$$\log p(\sigma_n, \theta) = (Y|0, K + \sigma_n^2 I) \tag{7}$$

To train the model, log marginal likelihood is maximized with respect to likelihood variance and kernel hyper parameters  $\theta$ .

GPR, implemented via the GPflow library [54], was employed for predictive modeling. This model posits that observed data points originate from an unknown function represented as a Gaussian process. This approach is particularly adept at capturing the intricate, non-linear relationship between relative density and mechanical/piezoresistive properties, a crucial factor for comprehending the behavior of 2D auxetic cellular structures. The kernel's hyperparameters underwent optimization by maximizing the log marginal likelihood via Scipy's optimization algorithm. This crucial step ensures the model's adeptness at fitting the data and its generalizability to novel, unseen data, establishing a robust predictive tool. The model's accuracy was further validated through residual analyses and comparison of model estimates with experimental averages. Visualization techniques were employed to elucidate the findings, including plots depicting the relationship between relative density and mechanical/piezoresistive properties, complete with confidence intervals, and graphs comparing model estimates with experimental averages.

## 3 Results and Discussion

#### 3.1 Material characterization

In this study, the density assessment of 3D printed samples utilizing PLA/CB yielded a value of  $1.21 \text{ g/cm}^3$ , slightly below the manufacturer's reported filament density of  $1.24 \text{ g/cm}^3$ . This observation aligns with expectations, as porosity induced by MEX is a commonly encountered challenge, with a relatively low porosity of approximately 2.5% in this case. Each specimen was individually weighed upon removal from the print bed, and their thickness (z-direction) was meticulously documented, while their in-plane dimensions (x- and y-directions) were evaluated within strict tolerances of  $50\pm0.5$  mm. The average thickness of all samples was determined to be  $1.2\pm0.1$  mm. During the printer calibration process, optical microscopy was regularly employed to monitor the surface quality of the printed cellular structures, with a particular focus on reducing gaps between deposited filament beads to minimize porosity. It is noteworthy that, as a caveat, the ligaments tended to exhibit slight over-extrusion, resulting in a slightly wider appearance than initially planned.

The lower surface of the printed specimens displayed uniform roughness attributed to the print bed, which distinctly contrasted with the upper surface where filament deposition occurred (Figure S3). While no voids were observed, minor filament strands were detected between individual ligaments due to deposition paths and filament exiting the nozzle. It is important to note that these filament strands do not contribute to the structural integrity of the specimens under study.

#### 3.1.1 Differential scanning calorimetry

Differential scanning calorimetry (DSC) analysis was conducted utilizing a DSC 25 instrument from TA Instruments to elucidate the thermal characteristics of the PLA/CB composite employed in this study. The primary objectives were to ascertain the glass transition temperature, melting temperature and crystallinity. To assess potential changes in crystallinity, samples were obtained both from the original filament and from a 3D printed specimen. Each sample underwent a heating process up to a temperature of 200 °C, with a controlled heating rate of 10 °C/min. Crystallinity was determined as  $X\% = (\Delta H/\Delta H_{H100}) \times 100$ , where  $\Delta H$  represents the melting enthalpy of the PLA/CB composite, and  $\Delta H_{H100}$  denotes the enthalpy of fusion for a polymer that is 100% crystalline, a value established at 93.7 J/g [55]. The calculated crystallinity, glass transition temperatures, and other relevant thermal properties are summarized in Table S2. Upon the initial heating cycle, the calculated crystallinity was

found to be 14.77% for the filament and 18.48% for the printed component, indicating an increase in crystallinity following the 3D printing process. Subsequently, after the second heating cycle, residual crystallinity levels were measured at 0.75% for the filament and 4.1% for the printed specimen. This observation suggests that the cooling rate of 10 °C/min was insufficient to facilitate complete recovery of the composite's crystalline structure. Furthermore, the glass transition temperatures were determined to be 62 °C for both the PLA/CB filament and the printed parts. Representative thermograms depicting these findings are presented in Figure S4.

#### 3.1.2 Scanning electron microscopy

Scanning electron microscopy (SEM) analysis was conducted on 3D printed PLA/CB specimens using a Hitachi SU8240 instrument with an acceleration voltage of 10 kV. To reveal the nanofillers on the surface, the samples were cryogenically fractured using liquid nitrogen. Subsequently, sputter coating with gold/palladium was employed to enhance surface conductivity and mitigate the charging effect on the sample's surface. The SEM images obtained revealed a surface of high quality, characterized by the absence of macroscale pores. A large number of particles, which correspond to carbon black, were discernible within the gray polymeric matrix, signifying a well-dispersed distribution of these fillers throughout the specimen (refer to Figure 4).

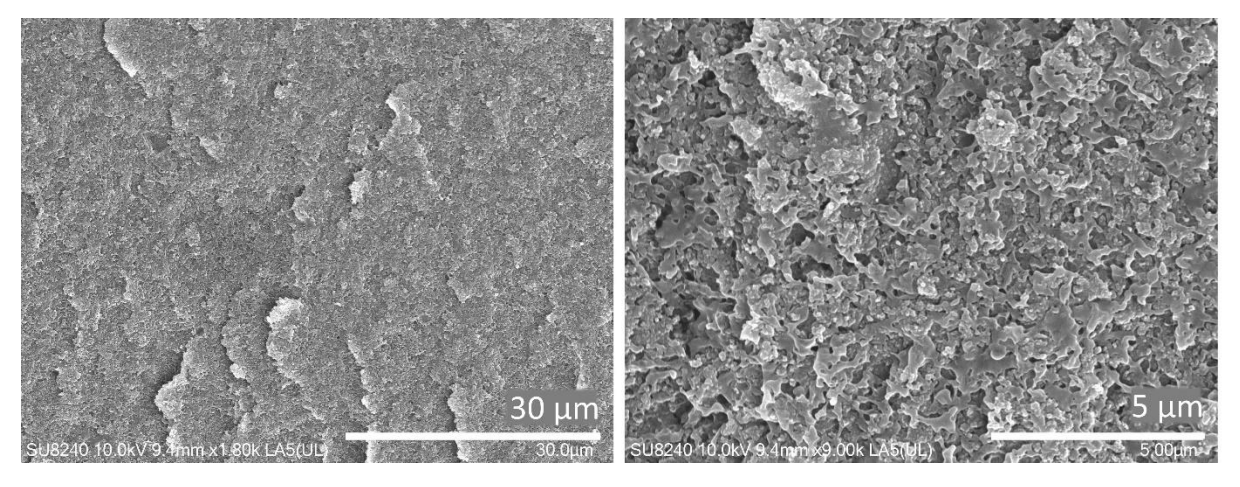


Figure 4. SEM analysis of a PLA/CB composite created through MEX. The left panel, captured at 1.80k magnification, depicts the cryogenic fracture surface texture. The right panel, at a higher magnification of 9.00k, reveals a granular morphology, suggestive of CB particulate presence within the polymer substrate.

#### 3.2 Mechanical and piezoresistive performances

#### 3.2.1 Mechanical and piezoresistive characteristics of parent nanocomposites

The bulk properties of PLA/CB composite were evaluated and are summarized in Table 1. The corresponding stress-strain behavior and the change in resistance as a function of strain for tensile, compression and flexural tests are depicted in Figure 5.

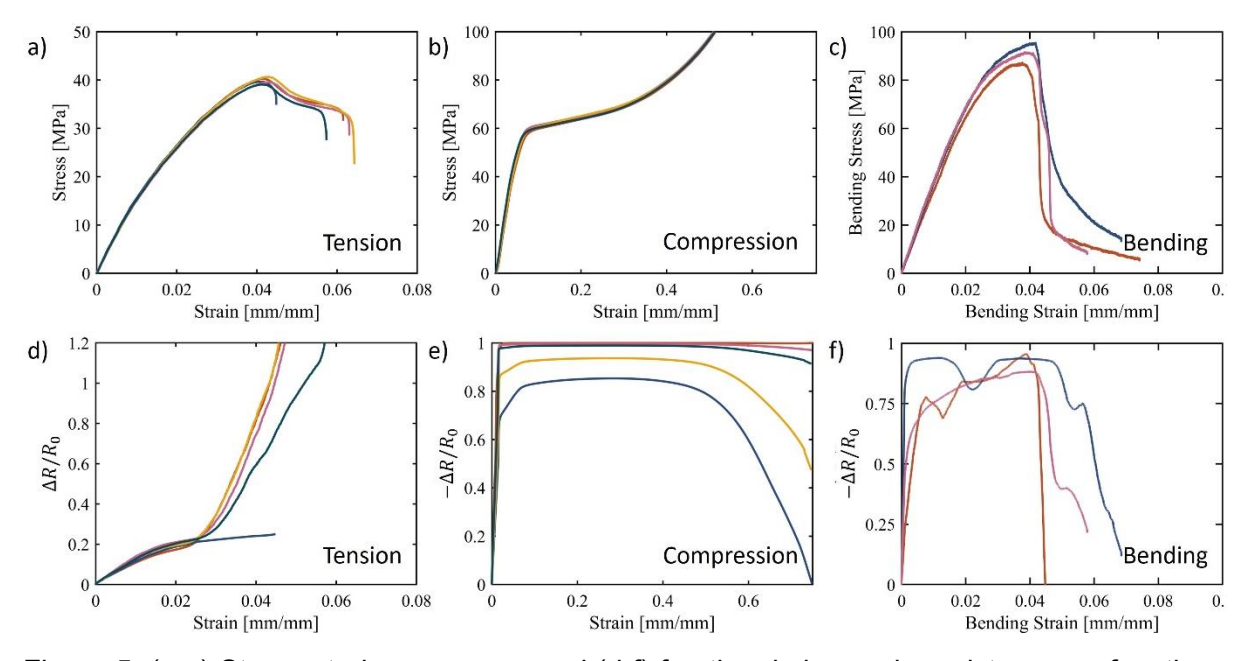


Figure 5. (a-c) Stress-strain responses and (d-f) fractional change in resistance as functions of strain for tensile, compression and three-point bending tests conducted on PLA/CB bulk specimens. The data is presented with three to five repetitions for each test condition.

Table 1. Bulk properties of PLA/CB under tensile, compression and flexural loadings

	Modulus [MPa]	Strength [MPa]	Toughness [MJ/m^3]	Gauge Factor [-]
Tension	1501 ± 17	40 ± 1	1.63 ± 0.28	12.4 ± 1.2
Compression	1278 ± 49	$64.5 \pm 0.5$	44.44 ± 0.23	50 ± 14.8
Bending	3603 ± 195	91 ± 4	3.15 ± 0.34	494 ± 290

The Young's modulus of the bulk material in tension was determined to be 1.5 GPa, which is higher than that in compression at 1.23 GPa. On the other hand, the strength in compression is significantly higher at 64 MPa compared to tension at 40 MPa. The flexural modulus, at 3.6 GPa, far exceeds the tensile and compressive moduli, although it should be similar to the tensile modulus under ideal elastic conditions. In reality, the stress-strain states in flexural and tensile tests differ because the maximum stress in tensile tests occurs throughout the

measurement volume, while in flexural tests, the maximum stresses are concentrated in small regions at the top and bottom of the specimen on opposite sides of the neutral layer. Since additively manufactured specimens are very sensitive to printing-induced defects, it is very likely and common that specimens tested under tensile loading will exhibit lower material properties than in flexure testing.

The gauge factor (measured over the elastic regime) for bulk composite in tension is low, with a value of 12.4, compared to compression and bending, which have values of 50 and 494, respectively. This finding corresponds to the initial electrical resistance measured at no load, which was on average 0.6 k $\Omega$ , 1.3 k $\Omega$ , and 117 k $\Omega$  for tension, compression, and bending, respectively. In tension, as strain increases, the distance between conducting paths in the polymer nanocomposites, here CB, also increases. This leads to a change in resistance, which is influenced not only by electron tunneling at CB-CB junctions but also by the contact resistance at these junctions. The contact resistance is important in determining the overall electrical resistance, especially as the physical separation between CB particles changes under strain. Consequently, the gauge factor, which indicates strain sensitivity in the elastic regime, tends to be lower than in the inelastic regime. In the latter, resistance changes are more influenced by inelastic processes such as damage and plasticity, further impacting the electrical properties of the nanocomposite [12]. During compression, at a certain critical strain, the CB network is altered, reducing the distance between conductive fillers and forming new conductive paths. Here, the change in electrical conductivity or resistance is mainly governed by the contact junction resistance between fillers, rather than electron tunneling. This morphological change in the conductive network is responsible for the observed resistance variations. In bending tests, the sensitivity of resistivity measurements to applied strain differs notably from that in uniaxial tension. The gauge factors in the elastic regime for bending are higher compared to those in uniaxial tension, and notably so in the initial elastic regime. This discrepancy is likely due to the differing stress distributions within the functional filler network in these testing conditions. In bending, unlike in uniform tension or compression, the material experiences both tensile and compressive stresses, leading to a non-uniform stress distribution and consequently altering the gauge factor [56]. Moreover, the piezoresistive response of materials is significantly influenced by how stress is distributed. Materials, particularly in additive manufacturing, often exhibit anisotropic properties. This anisotropy is especially pertinent in bending, where stress distribution is not uniform. Additionally, bending can induce localized high-strain areas, causing strain concentration effects that are less pronounced in uniform tension or compression. Various loading conditions lead to different microstructural changes in materials; for instance, bending might cause more substantial dislocation movements or crack formation compared to tension or compression. These

factors, along with potential surface stresses and contact effects with the universal testing machine in bending tests, can significantly influence the gauge factor.

#### 3.2.2 Mechanical and piezoresistive performance of nanoengineered auxetic lattices

In the pursuit of assessing the influence of unit cell topology (governed by architectural parameters of BSB structure) on both mechanical and piezoresistive properties, all cellular structures underwent tensile loading until reaching the point of complete failure. The stress-strain responses stemming from these experiments were plotted and analyzed to facilitate an in-depth understanding of the deformation and damage processes at play.

The stress-strain and resistance-strain histories for the various lattice structures subjected to tensile loading are presented in Figure 6 and Figure 7, respectively. Furthermore, the supplementary video 2 (SV2) contains an animated depiction of these results, including video footage of the experiments, thereby offering an enriched visual interpretation. All obtained results were normalized by the measured density of the individual structures. This normalization process served a dual purpose: firstly, to compensate for variations inherent in the printing process, and secondly, to facilitate the identification of superior-performing structures based on material utilization. As a result, the focus here is directed towards reporting weight-specific properties.

It is important to emphasize that the gauge factor in a lattice structure subjected to tension is governed by the modification in the morphology of the electrically percolated conductive network [57]. This modification results from both auxetic deformation and alterations in the resistivity of the cell walls within the lattice experiencing tension. As the lattice deforms under tensile stress, the electrically conductive pathways within the material are altered, impacting the overall electrical resistance of the structure. This phenomenon is particularly pronounced in auxetic structures, where the unfolding of ligaments leads to significant changes in the morphology of the conductive network. The intricate interplay between mechanical deformation and electrical resistance is a key aspect in understanding the piezoresistive performance of these cellular nanocomposites.

Furthering our understanding of the piezoresistive behavior, the slope of the  $\Delta R/R_0$  versus strain curve in the inelastic regime is indicative of the rate of conductive network destruction within the lattice [15]. This instantaneous slope, mathematically expressed as  $(1/R_0)(dR/d\epsilon)$ , signifies how rapidly the conductive networks deteriorate under tension, correlating directly with the failure of the cell walls within the lattice under far-field tension. A steeper slope is indicative of a faster breakdown of these networks and, consequently, a more rapid onset of

mechanical failure. This relationship underscores the delicate balance between mechanical integrity and electrical conductivity in these structures. By fine-tuning the topology of the lattice structure, considering both the composite material and relative density, the gauge factor and failure characteristics can be deliberately altered. This approach termed 'design for failure', enables the tailoring of both mechanical and electrical responses to specific application requirements.

A shared characteristic among all structures is the gradual unfolding and straightening of ligaments in the direction of applied loading, transitioning from an initially angled state. This behavior gives rise to an initial decrease in modulus, followed by a subsequent increase as elongation progresses, ultimately culminating in material yielding. Intriguingly, a stepwise failure pattern is consistently observed across all structures, stemming from the sequential breaking of ligaments under the applied tensile load. After reaching an initial peak load, a stress peak is registered, with values ranging between 0.64 and 4.37 MPa·dm³/kg for the least and most performing structures, respectively. Subsequently, a sharp decline ensues, resulting in a reduction of up to 90% in the original strength, manifesting within an elongation range of 3 to 18% on average.

The Poisson's ratio, presented as a function of strain up to the point of first ligament failure, is thoughtfully documented in Figure 8. Furthermore, all pertinent performance attributes derived from the tensile tests conducted on lattice structures reported as a function of relative density, can be found in supplementary Table S3, complemented by the representation in Figure S5. It is evident from the data that with an increase in relative density, there's a corresponding linear increase in stiffness, indicating enhanced material efficacy attributable to greater material utilization. Concurrently, an uptick in strength is also discernible, although the incremental gains appear to plateau beyond the 25% relative density threshold. A noteworthy observation across all structures is the strong correlation between the gauge factor and the stiffness and strength characteristics of the structures. Specifically, higher stiffness and strength are consistently associated with a higher gauge factor. Conversely, lattice structures exhibiting a higher negative Poisson's ratio, tend to display diminished mechanical performance and gauge factors. Within the range of relative densities investigated herein, the negative Poisson's ratio of lattices remains largely unaffected by changes in relative density. This outcome aligns with expectations, given that auxetic behavior in cellular structures undergoing tensile loading primarily hinges on the unfolding of ligaments until they are fully stretched, thereby attaining maximum strength. Consequently, structures characterized by a high negative Poisson's ratio tend to exhibit lower specific energy absorption efficiency, as stress increases as a function of strain, it remain modest and nearly linear. However, it's

important to note that specific energy absorbed, as measured up to the initial ligament rupture, can still manifest at commendable levels.

The gauge factor's dependence on the lattice unit cell architecture underlines the significance of designing for specific piezoresistive properties. By manipulating the lattice configuration, it is possible to tune not only the mechanical attributes such as stiffness and strength but also the piezoresistive characteristics, particularly the gauge factor. This tuning is crucial for applications where both mechanical performance and sensing capabilities are essential. The lattice structures that exhibit higher negative Poisson's ratios tend to demonstrate a more pronounced modification in the morphology of their conductive networks under tension, leading to distinct piezoresistive behaviors. This observation is vital for the development of advanced materials that require a precise balance between mechanical resilience and electrical response.

In the preliminary examination of tensile behavior, S1a emerges as a standout performer, boasting a superior specific modulus, strength, and gauge factor. At a relative density of 30%, S1a achieves peak values of 240.5 MPa·dm³/kg, 4.6 MPa·dm³/kg, and 15.3, respectively. Conversely, the Poisson's ratio for this structure approaches zero, registering an average of 0.1, indicative of minimal lateral expansion during testing. Efficiency calculations yield a value of 61%, slightly exceeding the average for tested structures. However, specific energy absorbed is comparatively lower, quantified at 73 J/kg. With a relative density of 10%, the modulus, strength and gauge factor continue to exhibit impressive properties, with the modulus and strength maintaining robust figures at 45 and 2 MPa·dm³/kg, respectively, and the gauge factor at 5.5. This underscores the material's consistent and strong performance across various density levels. In stark contrast, S1d exhibits notably inferior mechanical performance, with a specific modulus of 15.5 MPa·dm³/kg, amounting to only about 6.5% of S1a's stiffness at the same relative density. Specific strength and gauge factors mirror this subpar performance, while Poisson's ratio reaches an exceptionally low -0.62, marking one of the most pronounced instances of auxetic behavior among the observed structures.

While structures within shape set 1 display a pronounced inclination towards either robust mechanical resilience or a higher negative Poisson's ratio, this distinction becomes less discernible within shape sets 2 and 3. Specifically, the average specific stiffness for all tested relative densities and structures within set 1 is calculated at 54±62 MPa·dm³/kg. Comparatively, this metric yields values of 69±48 MPa·dm³/kg and 53±22 MPa·dm³/kg for shape sets 2 and 3, respectively. The noticeably reduced range in values reflects the influence of structural symmetry, with decreasing symmetry resulting in less extreme mechanical behavior and increased randomness. Striking a balance between commendable mechanical

properties and auxeticity, structures S2c and S2d emerge as noteworthy performers with energy absorption of up to 198 J/kg at only 10% relative density. These structures exhibit superior mechanical performance compared to S1d while maintaining an average Poisson's ratio of -0.67 and -0.54, respectively, across all densities.

Delving into the parameters governing geometry, it becomes apparent that both branch angle and branch length play pivotal roles in shaping overall structural performance. Structures characterized by branch angles of less than 90° in all four branches tend to exhibit exceptional mechanical strength, exemplified by S1a and S1b. Conversely, structures featuring branch angles of 90° or more across all branches excel in auxetic properties, typified by S1c and S1d. This clear relationship is most pronounced in structures with complete symmetry, as observed in shape set 1, where a single angle and length dictate structural characteristics. Structures within shape set 2, featuring two differently angled branches, strike a more harmonious balance between mechanical, electrical, and auxetic performance. In this scenario, increasing branch length while preserving stem length results in a notable enhancement of mechanical performance, as demonstrated by the contrasting behavior of S2b and S2c, where branch length is the sole variable altered. When four angles come into play, performance becomes less predictable but generally balanced, mirroring tendencies observed earlier, with inward angles enhancing performance and outward angles promoting auxeticity. Notably, a wellbalanced mixture of angles positively impacts specific energy absorption capacity and specific toughness, as evident in structures within shape set 3. Consequently, this study underscores the significance of deliberate angle and length selection in branch geometry, offering the potential for tailored outcomes in terms of stiffness, strength, and Poisson's ratio.

Finally, a composite score for each structure was evaluated by first normalizing the performance metrics across six categories: normalized Young's modulus and strength, gauge factor, energy absorbed and Poisson's ratio. Normalization was performed by subtracting the minimum value and dividing by the range of each category, thus rescaling the values to a 0-1 range. For Poisson's ratio, where a more negative value is preferable, the score was inverted by subtracting the value from the maximum and dividing by the range, effectively reversing the scale. The composite score for each structure was then calculated as the sum of these normalized values, providing a single figure representing the overall performance. These normalized values were then summed to calculate the composite score for each structure, providing a singular metric representing overall performance. Higher scores denote superior performance, as illustrated in Figure S6, where structure S2d is shown to distinctly outperform others with S2c and S1a closely trailing, each characterized by a relative density of 30%. The composite scores vary across the range of relative densities; therefore, mean composite

scores were computed for each subset by aggregating performance metrics across specimens. Figure S7 depicts these average scores, highlighting a comparable performance between S2c and S3d, topped only by S2d. S1a, however, ranks as the fourth noteworthy structure due to its lower Poisson's ratio, underscoring its specific performance characteristics under these analytical conditions.

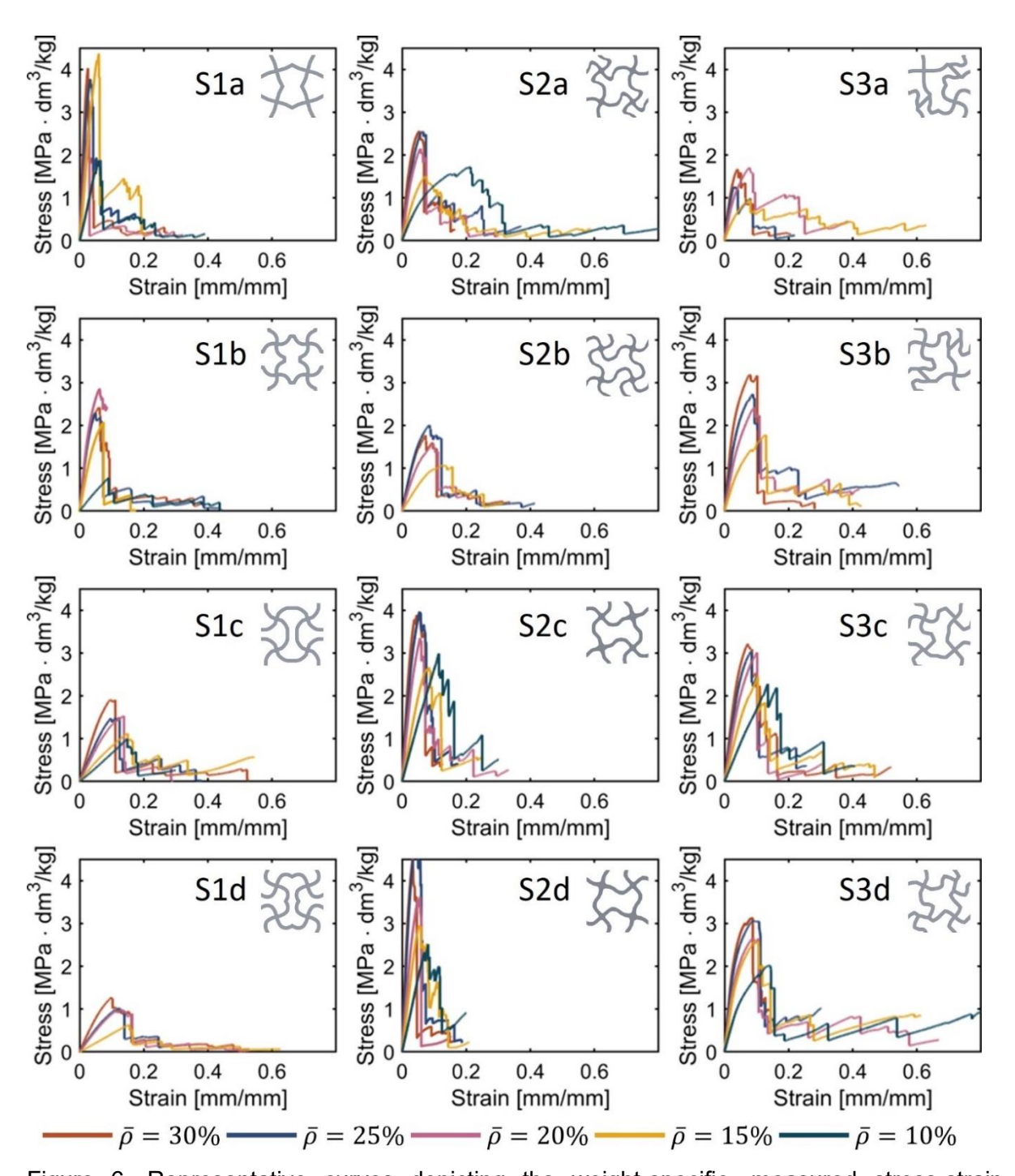


Figure 6. Representative curves depicting the weight-specific, measured stress-strain

response for various lattices under tensile loading across a range of relative densities.

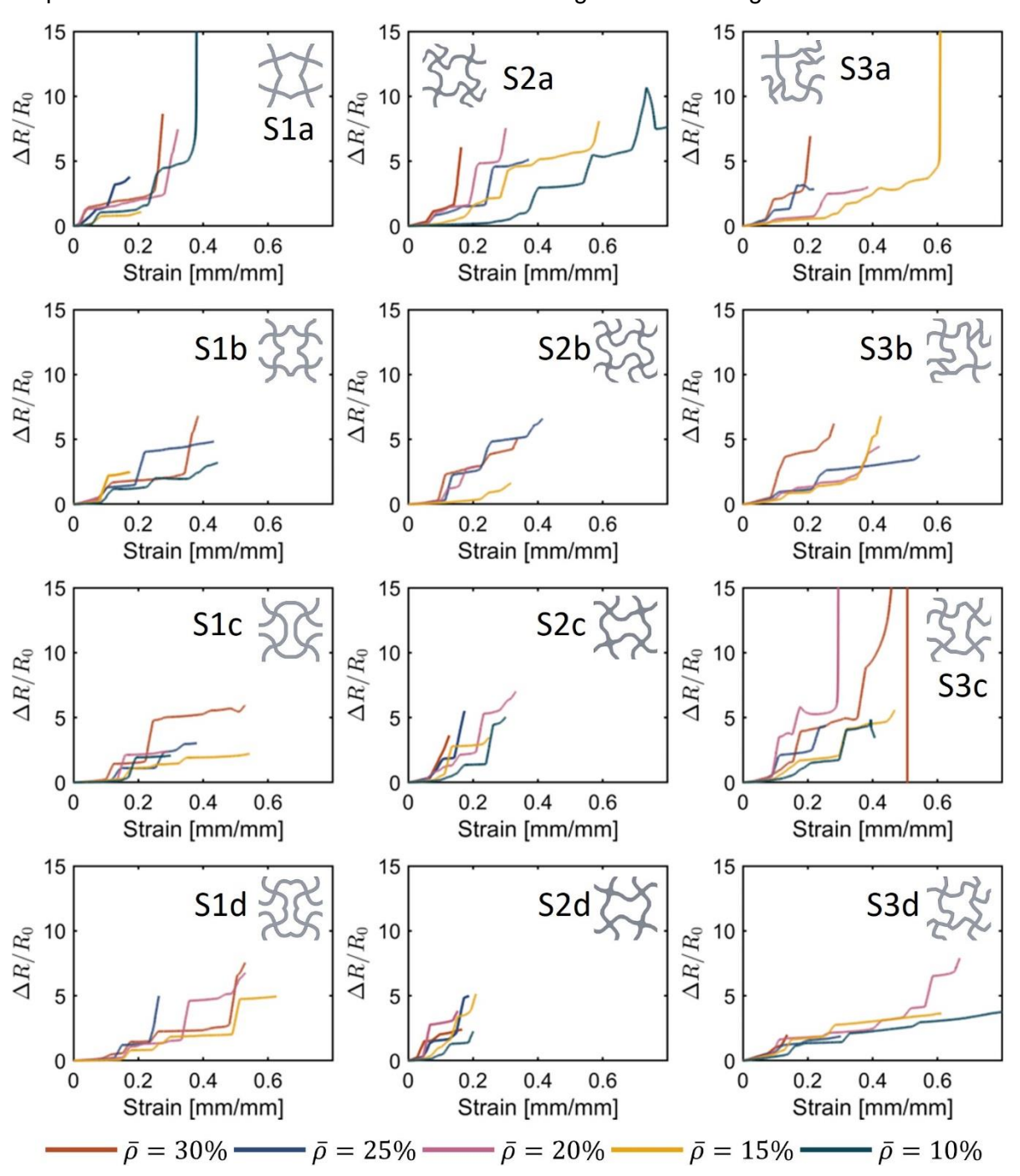


Figure 7. Representative curves of the measured relative change in electrical resistance as a function of strain for different architectures under tensile load for a spectrum of relative densities.

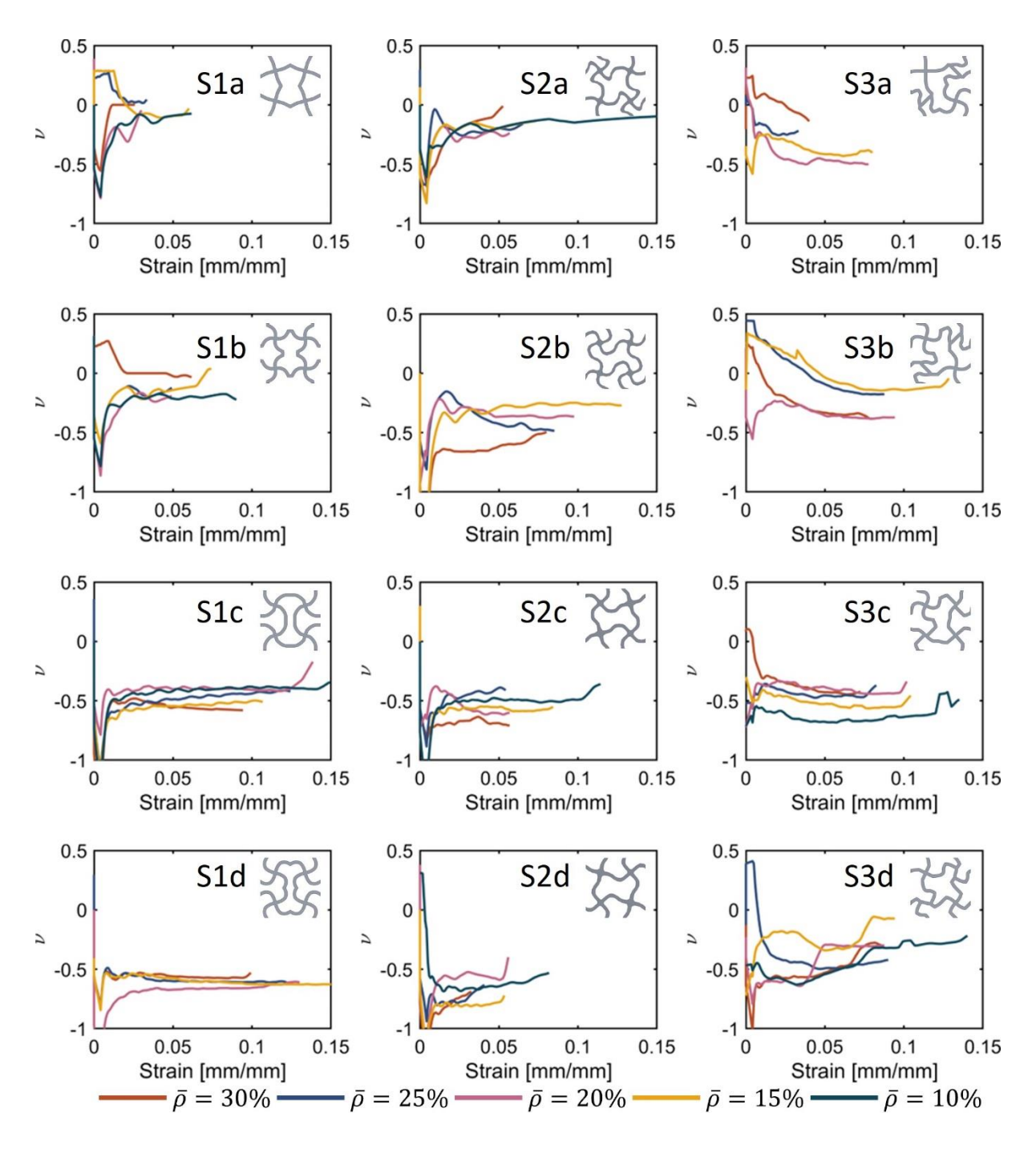


Figure 8. Representative curves of Poisson's ratio as a function of strain for different lattice structures under tensile load for the tested range of relative densities up to a strain at which the first ligament break occurs.

#### 3.3 Insights from finite element analysis

The outcomes of the FE analysis provide substantial corroborating evidence for the experimental results. Much akin to the experimental findings, the stepwise failure phenomenon was successfully replicated in the simulations. This is illustrated in Figure 9, where part (a) compares the stress-strain responses from FE analysis and experiments, and part (b) contrasts the deformation maps, delineating the FE analysis against experimental

deformation. Models S1a, S2d, and S3c were chosen for their exemplary representation of each symmetry group's mechanical response. However, it's worth noting that the precise locations of ligament breakage may exhibit variability between experiments and simulations. This variation was anticipated, considering that no two experiments displayed identical fracture patterns across all repetitions.

In all instances, tensile stress predominantly converges on the vertically oriented walls aligned with the loading direction, with the horizontal walls bearing significantly lesser loads. Within these vertically aligned walls, the stress peaks congregate in regions characterized by the highest curvature of the ligaments. This is the locus where the primary unfolding of the ligament transpires, consequently rendering these sites susceptible to ligament failure during prolonged elongation. The Von Mises stress values evaluated in the ligaments at 5% strain exhibited a range spanning from 23.9 MPa to 49.7 MPa across all structures. Notably, the maximum values were observed in S1c and S1d, serving as an informative indicator of the prevailing deformation mode, whether it be bending or stretching.

In structures primarily dominated by bending, deformation primarily arises from the unfolding mechanisms of the ligaments. Conversely, in structures dominated by stretching, the ligaments experience direct loading, resulting in elevated stresses within the individual walls. In most cases, the mechanical properties, including Young's modulus and strength, as determined through FEA, fall within a range consistent with the standard error as observed in experimental evaluations. However, certain structures, such as S2b or S1d, exhibited more complex geometries with sharp angles, providing greater scope for ligament unfolding. In these cases, while the unfolding mechanisms were well-captured in the simulations, reality demonstrated greater resistance, leading to higher stiffness and earlier ligament failure in comparison to the simulated predictions. Similar effects were observed in S2a, S2c, and S2d, where the simulation indicated slightly lower stiffness relative to experimental evaluation, but the maximum stress levels exceeded the experimentally determined values.

The variance observed in some instances, where elongation at break and absorbed energy surpassed experimental validations, while in other structures it did not, underscores the inherent limitations in predicting outcomes solely through FEA. Analogous findings concerning the intricate damage behavior of MEX processed PLA were documented and studied by Vanaei et al. [58]. Their research revealed a range of failure strains spanning from 7% to 2% for structures with one to three printed filament layers in the loading direction, and even 9.5% for PLA filament that had not undergone 3D printing processing. This discrepancy arises from the existence of systematic errors, even in a meticulously calibrated AM process. These errors pose challenges in establishing a predictive capability using the conventional FE framework

employed herein. Consequently, it is postulated that the integration of physics-informed machine learning methods may offer valuable support in enhancing the prediction of material properties, as elaborated upon in the ensuing section.

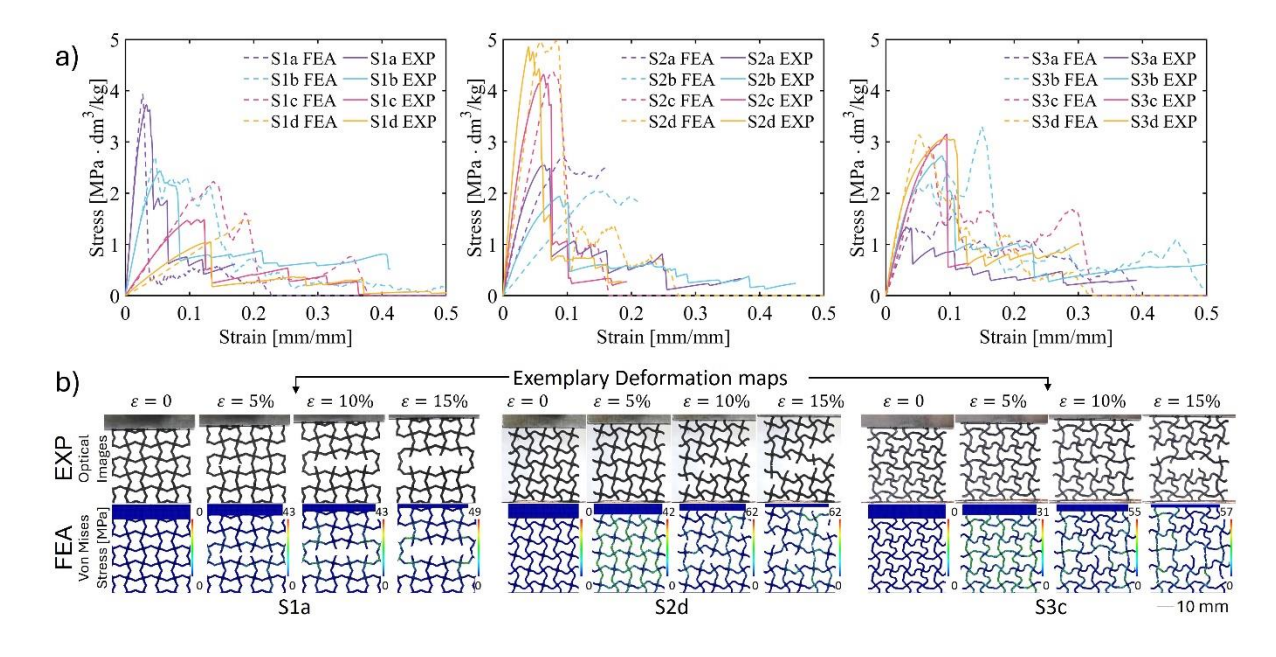


Figure 9. a) Representative curves of the weight-specific stress-strain response, and b) FEA vs experiments

#### 3.4 Data-driven performance prediction of auxetic structures

The GPR model is employed to predict mechanical and piezoresistive properties using experimental data. Its machine-learning-based framework also facilitates the inverse design of auxetic structures, allowing to stipulate desired mechanical and piezoresistive properties and subsequently reverse-engineer the corresponding structural parameters, including relative density. This capability is instrumental for designing and manufacturing 2D auxetic cellular structures with bespoke multifunctional properties. The analysis of tensile test data for 3D printed cellular structures, presented in the form of statistical variations and predictive models, reveals critical insights into the mechanical and piezoresistive self-sensing behavior of these auxetic lattices. The data, structured to illustrate variations in modulus, strength, and gauge factor as functions of relative density, are encapsulated by GPR results. The GPR, delineated by shaded confidence intervals in the graphs, extends the predictive capability of the model beyond the experimentally measured region, indicating its robustness in forecasting mechanical properties for untested densities (Figure 10, Figure S8).

The comparative graphs, which juxtapose experimental values against predictive models, elucidate the degree of congruence between observed and anticipated behaviors. A high correlation factor (R) for Young's modulus across the samples signifies a strong predictive

success, reaffirming the reliability of GPR in this context. For strength, the correlation is marginally lower, and the presence of outliers - attributed to the intricacies and inconsistencies inherent in the printing process - highlights the challenges in achieving uniformity in the printed structures. Furthermore, an increasing gauge factor with increasing modulus is observed, except for certain outliers. These deviations are not solely a consequence of the printing process but are also influenced by the incorporation and distribution of carbon black into the polymer matrix, which introduces additional complexity to the material's response. This relationship, while evident, is characterized by a more scattered distribution, suggesting that factors beyond relative density (e.g., distribution of CB in the PLA matrix) play a role in the gauge factor behavior.

The correlation factor serves as a quantifier of the precision of the predictive model. As such, lower R values for certain properties suggest a decrease in the predictive capability, particularly beyond the experimentally verified range. This uncertainty underscores the importance of experimental validation, especially when extending predictions into untested domains. In synthesizing these results, it becomes apparent that while the GPR model offers a sophisticated tool for predicting mechanical and sensing properties as a function of relative density, the confidence in these predictions varies. The correlation factors not only inform us about the past performance of the model but also guide expectations of its future applicability. This understanding is crucial in the context of material design, where the balance between predictive accuracy and experimental validation shapes the frontier of material innovation.

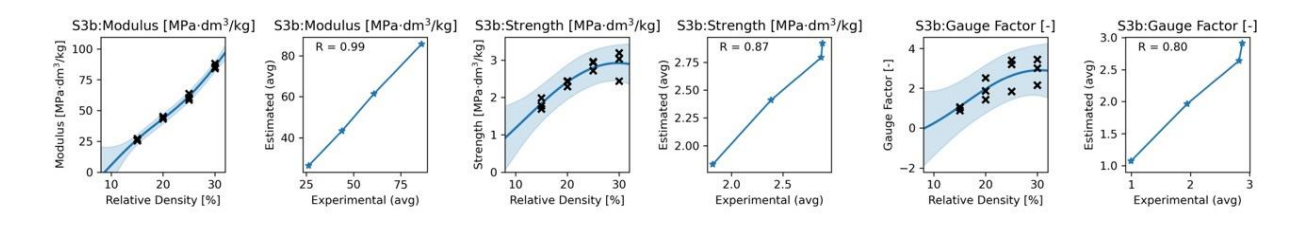


Figure 10. GP regression of mechanical and piezoresistive properties (Young's modulus, strength, and gauge factor) of 3D printed cellular structures (here for S3b, further graphs in Figure S8) as a function of relative density. The shaded areas represent the confidence intervals from Gaussian Process Regression, illustrating the predictive capability of the model. Subplots compare the experimental data (black crosses) with the GPR predictions (blue lines), where the correlation coefficient R quantifies the predictive accuracy.

# 4 Conclusions

This study focused on the development and multifunctional performance evaluation of 56 unique 2D auxetic lattice designs realized using conductive polylactic acid infused with carbon black via material extrusion. The lattice designs were developed using an innovative method

centered on control lines, combining Voronoi decomposition with p4 wallpaper symmetries. Finite element modeling and Gaussian Process Regression were employed to further explore and augment the property space. The study extensively explored the BSB structure's parameters such as stem length, branch angle, and branch length, thereby diversifying the design space to engineer lattice structures with required mechanical, electrical and piezoresistive properties.

Key findings highlight the significant influence of these parameters on the mechanical and piezoresistive properties of the cellular nanocomposites. The structures demonstrated auxetic behavior, with Poisson's ratios reaching as low as -0.74 in lattices like S2c, and specific strengths varying from 0.64 to 4.37 MPa dm<sup>3</sup>/kg. Notably, the Young's modulus and gauge factor varied significantly across the architectures, depending on the lattice design and relative density. For example, structure S1a at a 30% relative density exhibited a specific modulus of 240.5 MPa dm³/kg and a gauge factor of 15.3. In contrast, S1d, at the same relative density, demonstrated a lower specific modulus of 15.5 MPa·dm³/kg, illustrating a wide range of mechanical performance. These results represent up to a 15-fold increase in elastic stiffness and a 34-fold increase in gauge factor for the same relative density (same mass). The variation in lattice architecture, while maintaining the same relative density, distinctly influences the mode of failure within the inelastic regime, as evidenced by the varying stress-strain and resistance-strain responses. For example, the balance of branch angles greater than 90° and less than 90° achieved a more balanced mechanical and piezoresistive response, while fully symmetric structures tended towards extreme responses. This modification in failure behavior is closely aligned with the damage sensitivity observed from the piezoresistive performance of the lattices.

These findings distinctly demonstrate how varying lattice architectures and topology critically influence the mode of failure within the inelastic regime, a key observation aligned with the damage sensitivity observed in the piezoresistive responses. This interplay between structural design and functional response underpins the 'design for failure' concept, allowing for the deliberate engineering of lattice materials that not only meet specific mechanical thresholds but also exhibit tailored piezoresistive behaviors under stress. The correlation between the Poisson's ratio and other mechanical properties such as stiffness and strength were significant, indicating that higher negative Poisson's ratios often correspond to reduced mechanical performance and gauge factors. Structures S2c, S2d, and S3d exhibited superior energy absorption compared to fully symmetric structures. Additionally, when considering mean values across all relative densities, S2d, S2c, and S3d showed maximum performance. Finite Element Analysis supported measured mechanical performance, emphasizing stepwise

failure and stress concentration in vertically oriented walls under loading. Machine learning, specifically Gaussian Process Regression, exhibited high predictive accuracy for Young's modulus (R up to 0.99) but revealed complexities in predicting strength and gauge factor, influenced by factors beyond relative density.

This study significantly contributes to the development of multifunctional auxetic materials while establishing a comprehensive framework for the design and fabrication of 2D auxetic cellular structures with adaptable mechanical and piezoresistive characteristics. By concurrently adjusting the geometric and topological features of nanoengineered additively manufactured auxetic lattices, it introduces the concepts of "design for strain sensing ability" and "design for failure". This innovative approach allows for the creation of structures with tunable auxeticity, strain sensitivity, and damage sensitivity, offering substantial benefits across various fields such as aerospace engineering, biomedical devices, and smart wearable technology. The validity of these findings confirmed through multiscale experiments and data-driven prediction methods, carries significant implications for future advancements in applications requiring stretchable electrodes, sensors, and real-time health monitoring, representing a noteworthy stride in the development of multifunctional auxetic lattices.

# 5 Acknowledgements

SK would like to acknowledge partial financial support through Reinvigorating Research Award [No: 201644-05]. JS and SK acknowledge EPSRC DTA PhD studentship [Award No: EP/R513222/1]. This work was partially supported by the National Science Foundation (NSF) Award #2048182 (Engineering Design and Systems Engineering Program). Any opinions, findings, and conclusions or recommendations expressed in this material are those of the authors and do not necessarily reflect the views of the NSF.

# 6 References

- [1] I. Gibson, D.W. Rosen, B. Stucker, M. Khorasani, D. Rosen, B. Stucker, M. Khorasani, Additive manufacturing technologies, Springer, 2021.
- [2] X. Zheng, H. Lee, T. Weisgraber, M. Shusteff, J. DeOtte, E. Duoss, J. Kuntz, M. Biener, Q. Ge, J. Jackson, S. Kucheyev, N. Fang, C. Spadaccini, Ultralight, Ultrastiff Mechanical Metamaterials, Science 344 (2014) 1373–1377. https://doi.org/10.1126/science.1252291.
- [3] X. Yu, J. Zhou, H. Liang, Z. Jiang, L. Wu, Mechanical metamaterials associated with stiffness, rigidity and compressibility: A brief review, Prog. Mater. Sci. 94 (2018) 114–173. https://doi.org/10.1016/j.pmatsci.2017.12.003.

- [4] T. Tancogne-Dejean, M. Diamantopoulou, M. Gorji, C. Bonatti, D. Mohr, 3D Plate-Lattices: An Emerging Class of Low-Density Metamaterial Exhibiting Optimal Isotropic Stiffness, Adv. Mater. 30 (2018) 1803334. https://doi.org/10.1002/adma.201803334.
- [5] T. Maconachie, M. Leary, B. Lozanovski, X. Zhang, M. Qian, O. Faruque, M. Brandt, SLM lattice structures: Properties, performance, applications and challenges, Mater. Des. 183 (2019) 108137. https://doi.org/10.1016/j.matdes.2019.108137.
- [6] S. Kumar, S. Tan, L. Zheng, D.M. Kochmann, Inverse-designed spinodoid metamaterials, Npj Comput. Mater. 6 (2020) 73. https://doi.org/10.1038/s41524-020-0341-6.
- [7] M. Zaiser, S. Zapperi, Disordered mechanical metamaterials, Nat. Rev. Phys. 5 (2023) 679–688. https://doi.org/10.1038/s42254-023-00639-3.
- [8] A.A. Zadpoor, Mechanical meta-materials, Mater. Horiz. 3 (2016) 371–381. https://doi.org/10.1039/C6MH00065G.
- [9] H.M.A. Kolken, A.A. Zadpoor, Auxetic mechanical metamaterials, RSC Adv. 7 (2017) 5111–5129. https://doi.org/10.1039/C6RA27333E.
- [10] C. Coulais, E. Teomy, K. de Reus, Y. Shokef, M. van Hecke, Combinatorial design of textured mechanical metamaterials, Nature 535 (2016) 529–532. https://doi.org/10.1038/nature18960.
- [11] N.K. Choudhry, B. Panda, S. Kumar, In-plane energy absorption characteristics of a modified re-entrant auxetic structure fabricated via 3D printing, Compos. Part B Eng. 228 (2022) 109437. https://doi.org/10.1016/j.compositesb.2021.109437.
- [12] P. Verma, J. Ubaid, K.M. Varadarajan, B.L. Wardle, S. Kumar, Synthesis and Characterization of Carbon Nanotube-Doped Thermoplastic Nanocomposites for the Additive Manufacturing of Self-Sensing Piezoresistive Materials, ACS Appl. Mater. Interfaces 14 (2022) 8361–8372. https://doi.org/10.1021/acsami.1c20491.
- [13] J.J. Andrew, H. Alhashmi, A. Schiffer, S. Kumar, V.S. Deshpande, Energy absorption and self-sensing performance of 3D printed CF/PEEK cellular composites, Mater. Des. 208 (2021) 109863. https://doi.org/10.1016/j.matdes.2021.109863.
- [14] C. Chen, X. Wang, Y. Wang, D. Yang, F. Yao, W. Zhang, B. Wang, G.A. Sewvandi, D. Yang, D. Hu, Additive Manufacturing of Piezoelectric Materials, Adv. Funct. Mater. 30 (2020) 2005141. https://doi.org/10.1002/adfm.202005141.
- [15] J. Ubaid, J. Schneider, V.S. Deshpande, B.L. Wardle, S. Kumar, Multifunctionality of Nanoengineered Self-Sensing Lattices Enabled by Additive Manufacturing, Adv. Eng. Mater. 24 (2022) 2200194. https://doi.org/10.1002/adem.202200194.
- [16] I. Sanz-Pena, M. Hopkins, N.R. Carrero, H. Xu, Embedded Pressure Sensing Metamaterials Using TPU-Graphene Composites and Additive Manufacturing, IEEE Sens. J. 23 (2023) 16656–16664. https://doi.org/10.1109/JSEN.2023.3283460.
- [17] J. Schneider, S. Basak, Y. Hou, J.H. Koo, B.L. Wardle, N. Gadegaard, S. Kumar, 3D-Printed Polyetheretherketone Smart Polymer Nanocomposite Scaffolds: Mechanical, Self-Sensing, and Biological Attributes, Adv. Eng. Mater. n/a (n.d.) 2301659. https://doi.org/10.1002/adem.202301659.
- [18] X. Ren, R. Das, P. Tran, T.D. Ngo, Y.M. Xie, Auxetic metamaterials and structures: a review, Smart Mater. Struct. 27 (2018) 023001. https://doi.org/10.1088/1361-665X/aaa61c.
- [19] S. Ji, L. Li, H.B. Motra, F. Wuttke, S. Sun, K. Michibayashi, M.H. Salisbury, Poisson's Ratio and Auxetic Properties of Natural Rocks, J. Geophys. Res. Solid Earth 123 (2018) 1161–1185. https://doi.org/10.1002/2017JB014606.
- [20] N.R. Keskar, J.R. Chelikowsky, Negative Poisson ratios in crystalline SiO2 from first-principles calculations, Nature 358 (1992) 222–224. https://doi.org/10.1038/358222a0.
- [21] Q. Liu, Literature Review: Materials with Negative Poisson's Ratios and Potential Applications to Aerospace and Defence, Aust Gov Dep Def (2006).
- [22] D. Acuna, F. Gutiérrez, R. Silva, H. Palza, A.S. Nunez, G. Düring, A three step recipe for designing auxetic materials on demand, Commun. Phys. 5 (2022) 1–9. https://doi.org/10.1038/s42005-022-00876-5.

- [23] D. Rayneau-Kirkhope, Stiff auxetics: Hierarchy as a route to stiff, strong lattice based auxetic meta-materials, Sci. Rep. 8 (2018) 12437. https://doi.org/10.1038/s41598-018-30822-x.
- [24] Y. Suzuki, G. Cardone, D. Restrepo, P.D. Zavattieri, T.S. Baker, F.A. Tezcan, Self-assembly of coherently dynamic, auxetic, two-dimensional protein crystals, Nature 533 (2016) 369–373. https://doi.org/10.1038/nature17633.
- [25] B. Jang, S. Won, J. Kim, J. Kim, M. Oh, H.-J. Lee, J.-H. Kim, Auxetic Meta-Display: Stretchable Display without Image Distortion, Adv. Funct. Mater. 32 (2022) 2113299. https://doi.org/10.1002/adfm.202113299.
- [26] J. Pan, Y.-F. Zhang, J. Zhang, H. Banjade, J. Yu, L. Yu, S. Du, A. Ruzsinszky, Z. Hu, Q. Yan, Auxetic two-dimensional transition metal selenides and halides, Npj Comput. Mater. 6 (2020) 1–6. https://doi.org/10.1038/s41524-020-00424-1.
- [27] J.H. Park, H.-J. Park, S.J. Tucker, S.K. Rutledge, L. Wang, M.E. Davis, S.J. Hollister, 3D Printing of Poly-ε-Caprolactone (PCL) Auxetic Implants with Advanced Performance for Large Volume Soft Tissue Engineering, Adv. Funct. Mater. 33 (2023) 2215220. https://doi.org/10.1002/adfm.202215220.
- [28] Y. Zhu, D. Gao, Y. Shao, H. Chen, C. Yu, Q. Wang, A novel prefabricated auxetic honeycomb meta-structure based on mortise and tenon principle, Compos. Struct. 329 (2024) 117782. https://doi.org/10.1016/j.compstruct.2023.117782.
- [29] L. Yang, O. Harrysson, H. West, D. Cormier, Mechanical properties of 3D re-entrant honeycomb auxetic structures realized via additive manufacturing, Int. J. Solids Struct. 69–70 (2015) 475–490. https://doi.org/10.1016/j.ijsolstr.2015.05.005.
- [30] J.N. Grima, R. Gatt, P.-S. Farrugia, On the properties of auxetic meta-tetrachiral structures, Phys. Status Solidi B 245 (2008) 511–520. https://doi.org/10.1002/pssb.200777704.
- [31] C.S. Ha, M.E. Plesha, R.S. Lakes, Chiral three-dimensional lattices with tunable Poisson's ratio, Smart Mater. Struct. 25 (2016) 054005. https://doi.org/10.1088/0964-1726/25/5/054005.
- [32] J.N. Grima, K.E. Evans, Auxetic behavior from rotating squares, J. Mater. Sci. Lett. 19 (2000) 1563–1565. https://doi.org/10.1023/A:1006781224002.
- [33] W. Jiang, X. Ren, S.L. Wang, X.G. Zhang, X.Y. Zhang, C. Luo, Y.M. Xie, F. Scarpa, A. Alderson, K.E. Evans, Manufacturing, characteristics and applications of auxetic foams: A state-of-the-art review, Compos. Part B Eng. 235 (2022) 109733. https://doi.org/10.1016/j.compositesb.2022.109733.
- [34] J.-H. Oh, J.-S. Kim, V.H. Nguyen, I.-K. Oh, Auxetic graphene oxide-porous foam for acoustic wave and shock energy dissipation, Compos. Part B Eng. 186 (2020) 107817. https://doi.org/10.1016/j.compositesb.2020.107817.
- [35] M. Razbin, M. Jamshidi Avanaki, A.A.A. Jeddi, H. Dabiryan, A systematic study on the predictability of different methods to predict the maximum Poisson's ratio of helical auxetic yarn, J. Text. Inst. 113 (2022) 90–100. https://doi.org/10.1080/00405000.2020.1863570.
- [36] Y. Zhu, Y. Luo, D. Gao, C. Yu, X. Ren, C. Zhang, In-plane elastic properties of a novel re-entrant auxetic honeycomb with zigzag inclined ligaments, Eng. Struct. 268 (2022) 114788. https://doi.org/10.1016/j.engstruct.2022.114788.
- [37] F. Lu, T. Wei, C. Zhang, Y. Huang, Y. Zhu, X. Rui, A novel 3D tetra-missing rib auxetic meta-structure with tension/compression-twisting coupling effect, Thin-Walled Struct. 199 (2024) 111764. https://doi.org/10.1016/j.tws.2024.111764.
- [38] Ó. Lecina-Tejero, M.Á. Pérez, E. García-Gareta, C. Borau, The rise of mechanical metamaterials: Auxetic constructs for skin wound healing, J. Tissue Eng. 14 (2023) 20417314231177838. https://doi.org/10.1177/20417314231177838.
- [39] N. Ravirala, A. Alderson, K.L. Alderson, P.J. Davies, Expanding the range of auxetic polymeric products using a novel melt-spinning route, Phys. Status Solidi B 242 (2005) 653–664. https://doi.org/10.1002/pssb.200460384.

- [40] L. Ren, W. Wu, L. Ren, Z. Song, Q. Liu, B. Li, Q. Wu, X. Zhou, 3D Printing of Auxetic Metamaterials with High-Temperature and Programmable Mechanical Properties, Adv. Mater. Technol. n/a (n.d.) 2101546. https://doi.org/10.1002/admt.202101546.
- [41] A.L. Loeb, Space-filling Polyhedra, in: A.L. Loeb (Ed.), Space Struct., Birkhäuser, Boston, MA, 1991: pp. 127–132. https://doi.org/10.1007/978-1-4612-0437-4\_16.
- [42] E. Akleman, V.R. Krishnamurthy, C.-A. Fu, S.G. Subramanian, M. Ebert, M. Eng, C. Starrett, H. Panchal, Generalized abeille tiles: Topologically interlocked space-filling shapes generated based on fabric symmetries, Comput. Graph. 89 (2020) 156–166. https://doi.org/10.1016/j.cag.2020.05.016.
- [43] T. Yildiz, E. Akleman, V. Krishnamurthy, M. Ebert, A modular approach for creation of any bi-axial woven structure with congruent tiles, Comput. Graph. 114 (2023) 357–367. https://doi.org/10.1016/j.cag.2023.06.017.
- [44] M. Ebert, E. Akleman, V. Krishnamurthy, R. Kulagin, Y. Estrin, VoroNoodles: Topological Interlocking with Helical Layered 2-Honeycombs, Adv. Eng. Mater. n/a (n.d.) 2300831. https://doi.org/10.1002/adem.202300831.
- [45] M. Ebert, R. Adhikari, M.K. Hasan, K. Lupo, E. Akleman, M. Pharr, V.R. Krishnamurthy, ABC-Auxetics: An Implicit Design Approach for Negative Poisson's Ratio Materials, Adv. Eng. Mater. n/a (n.d.). https://doi.org/10.1002/adem.202301359.
- [46] S. Domaschke, A. Morel, G. Fortunato, A.E. Ehret, Random auxetics from buckling fibre networks, Nat. Commun. 10 (2019) 4863. https://doi.org/10.1038/s41467-019-12757-7.
- [47] Technical Data Sheet Rev 1. Conductive PLA, (n.d.). http://www.farnell.com/datasheets/3179312.pdf (accessed August 19, 2021).
- [48] J. Schneider, S. Kumar, Multiscale characterization and constitutive parameters identification of polyamide (PA12) processed via selective laser sintering, Polym. Test. 86 (2020) 106357. https://doi.org/10.1016/j.polymertesting.2020.106357.
- [49] D. Atilla Yolcu, B. Okutan Baba, Measurement of Poisson's ratio of the auxetic structure, Measurement 204 (2022) 112040. https://doi.org/10.1016/j.measurement.2022.112040.
- [50] Extended Drucker-Prager Models SIMULIA User Assistance 2023, (n.d.). https://help.3ds.com/2023/english/dssimulia\_established/SIMACAEMATRefMap/simam at-c-druckerprager.htm?contextscope=all (accessed June 20, 2023).
- [51] M.F.F. Arif, S. Kumar, K.M.K. Varadarajan, W.J.J. Cantwell, Performance of biocompatible PEEK processed by fused deposition additive manufacturing, Mater. Des. 146 (2018) 249–259. https://doi.org/10.1016/j.matdes.2018.03.015.
- [52] M.F. Arif, H. Alhashmi, K.M. Varadarajan, J.H. Koo, A.J. Hart, S. Kumar, Multifunctional performance of carbon nanotubes and graphene nanoplatelets reinforced PEEK composites enabled via FFF additive manufacturing, Compos. Part B Eng. 184 (2020) 107625. https://doi.org/10.1016/j.compositesb.2019.107625.
- [53] C. Rasmussen, O. Bousquet, U. Luxburg, G. Rätsch, Gaussian Processes in Machine Learning, Adv. Lect. Mach. Learn. ML Summer Sch. 2003 Canberra Aust. Febr. 2 - 14 2003 Tüb. Ger. August 4 - 16 2003 Revis. Lect. 63-71 2004 3176 (2004). https://doi.org/10.1007/978-3-540-28650-9\_4.
- [54] A.G. de G. Matthews, M. van der Wilk, T. Nickson, K. Fujii, A. Boukouvalas, P. Le{\'o}n-Villagr{\'a}, Z. Ghahramani, J. Hensman, GPflow: A Gaussian Process Library using TensorFlow, J. Mach. Learn. Res. 18 (2017) 1–6.
- [55] D. Garlotta, A Literature Review of Poly(Lactic Acid), J. Polym. Environ. 9 (2001) 63–84. https://doi.org/10.1023/A:1020200822435.
- [56] M.U. Azam, A. Schiffer, S. Kumar, Mechanical and piezoresistive behavior of selectively laser sintered MWCNT/UHMWPE nanocomposites, Compos. Part Appl. Sci. Manuf. 173 (2023) 107701. https://doi.org/10.1016/j.compositesa.2023.107701.
- [57] A. Mora, P. Verma, S. Kumar, Electrical conductivity of CNT/polymer composites: 3D printing, measurements and modeling, Compos. Part B Eng. 183 (2020) 107600. https://doi.org/10.1016/J.COMPOSITESB.2019.107600.

[58] H.R. Vanaei, M. Shirinbayan, S. Vanaei, J. Fitoussi, S. Khelladi, A. Tcharkhtchi, Multi-scale damage analysis and fatigue behavior of PLA manufactured by fused deposition modeling (FDM), Rapid Prototyp. J. 27 (2021) 371–378. https://doi.org/10.1108/RPJ-11-2019-0300.